DIRECT NUMERICAL SIMULATIONS OF COHERENT STRUCTURES IN WAVE BOUNDARY LAYER

A Thesis

Presented to the Faculty of the Graduate School

of Cornell University

in Partial Fulfillment of the Requirements for the Degree of

Master of Science

by

Chen-Pey Huang

January 2011

ABSTRACT

In this study, a high-resolution and high-accuracy 2D pseudo-spectral numerical model (Diamessis *et al*. 2005) [23] is applied to investigate the boundary layer flows under a surface solitary wave. The numerical results are compared with the analytical solution derived by Liu & Orfilla (2004)[24], and the experimental data obtained from a series of U-tube experiments provided by Sumer *et al*. (2010)[21]. Define the Reynolds number as Re = aU_{0m}/ν, where U_{0m} is the maximum free-stream velocity, $2a$ the corresponding fluid particle displacement, and ν the fluid viscosity, Sumer *et al*. (2010)[21] tested the boundary layer flow under the soliton-like pressure gradient for Re ranging from 2.8×10^4 to 2.0×10^6. They reported that as the Reynolds number increases, the boundary flow experiences from laminar regime to the transitional flow regime where a regular array of 2D vortex tubes was generated in the boundary layer; and then to the turbulent flow regime where the 3D turbulent spots appear. In this study, we design three cases following the Sumer *et al*. (2010)'s[21] experimental setup in the transitional flow regime (Re ranging from 2.0×10^5 to 6.0×10^5) to examine the characteriscs and the evolution of the vortex coherent structures in the wave boundary layer. An universal graph of the evolution of the normalized bed shear stress without generalization of the vortex tubes within different Reynolds number is shown as a preliminary discuss of the near-bed flow behaviour. The vortex coherent structures are then triggered by inserting numerical noises, we conclude that during the deceleration stage, flow reversal occurs near the boundary layer, the Kevin-Helmholz (K-H) instability is found to be the main mechanism responsible for the generation of the 2D vortex tubes.

The evolution of the shear layer instability is examined and discussed. The evolution of the shear layer instability is also provided in this study by examing the development of the vortex structures and the spatio-temporal description of the bottom shear stress. The changes of the vorticity field are quantified by vortex tube characteristics, such as the magnitude, size and trajectory. To investigate the effect of tsunami-typed surface wave on the coherent structure in boundary layer, a further study applying the non-symmetric surface solitary wave is also provided.

BIOGRAPHICAL SKETCH

The author was born in Taipei, Taiwan. He went to National Chiao-Tung University in 1994 and graduated in 1998 with a bachelor degree from the Department of Civil Engineering. He enrolled in a post-graduate program in the same university in the Environmental department focusing on numerical analysis in groundwater flow and transport. After he received his Master of Science degree in 2000, he went to work in National Center for High-performance compuiting in Taiwan. He works for 6 years and then he wen to Cornell University in the major of Environmental Fluid Mechanics and Hydrology. His research areas at Cornell University include numerical analysis in wave-structure-foundation interaction and boundary layer flow under a solitary wave.

To my parents

ACKNOWLEDGEMENTS

I want to express my gratitude to my advisor, Professor Philip L.-F. Liu, for his help and support in my study at Cornell. I also want to thank my thesis committee members, Professor Peter J. Diamessis at School of Civil and Environmental Engineering and Professor Lance Collins at School of Mechanical and Aerospace Engineering, for their valuable advice on my course work and insightful comments on my thesis study. I also want to thank to everyone who help me during the 4 year study. Finally, I like to express the gratitude from my heart to my parents, who have been giving me the invaluable and endless support in my life.

TABLE OF CONTENTS

LIST OF TABLES

LIST OF FIGURES

CHAPTER 1

INTRODUCTION

1.1 Background

Coastal environments are vulnerable to three possible natural disasters, namely, tsunami, storm surge, and high wave attack due to storms (Shibayama 2009)[27]. Recently, natural disasters caused by tsunamis are widely reported around the world. Between 1933 and 1983, there were several big tsunamis caused by earthquakes in the vincinty of the Japanese island. In 1960, there was a big earthquake in the offshore sea of Chili, which lead a severe damage, the generated tsunami even traveled through the pacific ocean and effects on the East Asian were reported. In December 2004, there was the Indian Ocean tsunami, which was caused by an earthquake of surface wave magnitude (Ms) 9.0 occurred off the west coast of northern Sumatra. Severe damage was reported by countries around the Bay of Bendal and the Indian Ocean including Indonesia, Thailand, Sri Lanka and India. More than 150,000 deathes in total were reported by 11 nations, with and additional 80,000 missing. Considering the damage and change of topography made by the tsunami, the 2004 Indian Ocean Tsunamis left behind widespread of sediment deposits (Liu *et al*. 2005[25]; Yeh *et al*. 2007[13]). Large amount of sediments on the seafloor were suspended and transported by the tsunami and deposited to the beach, which might destroy facilities along the seashore and cause damages to the environment. Therefore, the study of tusnami behavior, monitoring, protection and forecasting has become a major engineering issue in recent years.

Tsunamis are caused by submarine earthquakes or submarine landslides in

the continental shelf or coastal zones. There are usually several waves come along with the tsunamis. The leading wave of tsunamis can be characterized as transient long waves, specifically, the non-symmetric type surface solitary waves, as they usually come with a longer deceleration wave period. Sometimes there is only the water surface raising for the acceleration stage and coming along with the constant water level a single uniform bore for the deceleration stage. But of the research interests, it would be fundemental to first look at the symmetric-typed surface solitary wave first, to get a first understanding of the tsunamis.

To further understand the forming mechanism, traveling time, and recurrence interval of tsunamis, it would be interesting to look at the corelation of the properties of tsunami sediment deposits with the flow depth, velocity and other wave mechanics (Huntington *et al*. 2007[15]; Jankaew *et al*. 2008[16]). This can improve the tsunami assessment, which will help build the tsunami database and improve the forecast and protection system. To describe the mechanism of the sediment transported by tsunamis is then one important issue. In this study, the turbulent flow on the bottom boundary layer with a tsunami-type surface solitary wave is considered, to discuss the roll-up of the vortex structures that can raise the sediment on the sea floor and bring it to the beach.

1.2 Solitary wave

Before the study of the boundary layer flow under surface solitary wave, it would be interesting to review the solitary wave property first. A solitary wave is a single wave with single crest whose amplitude diminishes to zero as hori-

zontal distance goes to infinity. It is a special kind of finite-amplitude wave in shallow water, and can be defined from cnoidal wave thory by the water depth and the wave height, where the wave period is infinity. The surface elevation of the solitary wave is defined as[22],[6],[18]:

$$\eta(\theta) = H sech^2(\theta) \tag{1.1}$$

where H is the wave height and θ, the phase, is defined as:

$$\theta(x,t) = \sqrt{\frac{3H}{4h^3}}(ct - x) \tag{1.2}$$

h is the water depth, c is the phase velocity and is defined by:

$$c = \sqrt{gh(1 - \frac{H}{h})} \tag{1.3}$$

Applying potential flow theory, the horizontal velocity is:

$$U(\eta, z) = \sqrt{gh}[\frac{\eta}{h} - (\frac{\eta}{2h})^2 + (\frac{1}{3} - \frac{1}{2}(\frac{z+h}{h})^2)h\eta_{xx}] \tag{1.4}$$

The horizontal free stream velocity, U_0, is found using z = -h. When substituting θ into the surface elevation equation, and assuming small amplitude waves, $\frac{\eta}{h}$, $\frac{H}{h}$, and $h\eta_{xx}$ can be taking as small quantities, the horizontal free stream velocity becomes:

$$U_0(x,t) = \sqrt{gh}\frac{H}{h} sech^2(\sqrt{\frac{3H}{4h^3}}(ct - x)) \tag{1.5}$$

For x = 0, the free stream velocity can be written as:

$$U_0(t) = U_{0m} sech^2(\omega\tau) \tag{1.6}$$

with

$$U_{0m} = \frac{H}{h}\sqrt{gh}, \omega = \frac{\sqrt{\frac{3gH}{4}}}{h}, T = \frac{2\pi}{\omega}, \ \ and\ \tau = t - t_0 \tag{1.7}$$

in which U_{0m} is the maximum free stream velocity. ω and T gives the time scale of a solitary wave event. t=t_0 or $\tau = 0$ is the time when the free stream velocity reaches its maximum value and the time profile of the free stream velocity is symmetric with respect to $\tau = 0$. The pressure gradient can be found as the major driving force in the boundary layer by looking at the streamwise component (x-direction) of the Navier-Stokes equation. Inside the water column, the velocity is mainly a horizontal flow, which means that the vertical velocity is zero. This indicates that the length scales in the x-direction are large compared to the scales in the z-direction. This gives:

$$\frac{\partial}{\partial z} = 0 \tag{1.8}$$

As inside the U-tube, the horizontal velocity is uniform at each elevation, this gives:

$$\frac{\partial U_0}{\partial x} = 0 \tag{1.9}$$

Now revisit the streamwise component of the 2-D Navier-Stokes equation (in x-z):

$$\frac{\partial U_0}{\partial t} + U_0\frac{\partial U_0}{\partial x} + w\frac{\partial U_0}{\partial z} = -\frac{1}{\rho}\frac{\partial p}{\partial x} + \nu\frac{\partial^2 U_0}{\partial x^2} + \nu\frac{\partial^2 U_0}{\partial z^2} \tag{1.10}$$

This equation can be simplified as:

$$\frac{\partial p}{\partial x} = -\rho\frac{\partial U_0}{\partial t} \tag{1.11}$$

Which also indicates that the pressure gradient drives the free stream velocity, and can be caluclated as:

$$\frac{1}{\rho}\frac{\partial p}{\partial x} = -\frac{\partial U_0}{\partial t} = 2U_{0m}\omega\mathrm{sech}^2(\omega\tau)\tanh(\omega\tau) \tag{1.12}$$

Time history of the free stream velocity and the pressure gradient can be seen in figure 1.1. The phase is from $\omega\tau$ = -180° to $\omega\tau$ = 180°, the solid line represents the free stream velocity, the dash line is the pressure gradient. The free stream velocity is rescaled by the maximum free stream velocity U_{0m}, and the pressure gradient is rescaled by $U_{0m}\omega$. Figure 1.1 shows that from $\omega\tau$ = -180° to $\omega\tau$ = 0°, the free stream velocity is increasing with time, after $\omega\tau$ = 0°, the free stream velocity decreases with time. This means that during the first stage, the free stream is accelerated by the solitary wave and can be taken as the acceleration stage, while during the scond stage, the solitary wave slows down the free stream, therefore can be taken as the deceleration stage.

1.3 Wave boundary layer study

Several studies have been reported on the analyses of boundary layer flow under the transient long wave, including solitary waves. Liu & Orfila (2004)[24] derived analytical solutions for viscous boundary layer flows under a weekly nonlinear transient wave. They showed that the perturbation boundary layer velocity satisfies the linear diffusion equation and the total boundary layer velocity can be written as:

$$u(x,\eta,t) = -\frac{\eta}{\sqrt{2\pi}} \int_0^t \frac{u_\omega(x,t)}{\sqrt{(t-\tau)^3}} exp[\frac{-\eta^2}{4(t-\tau)}]\, d\tau \tag{1.13}$$

where u_τ is the free stream velocity at the outer edge of the boundary layer and can be determined from a potential flow theory and η represents the coordinate normal to the seabed pointing toward the interior. The corresponding bottom shear stress can be calculated from the following formula (Liu & Orfila 2004)[24]:

$$\tau_b(x,t) = \frac{1}{\sqrt{\pi}} \int_0^t \frac{\partial u_\omega(x,t)/\partial\tau}{\sqrt{(t-\tau)}}\, d\tau \tag{1.14}$$

The bottom shear stress is a convolution integral of the fluid particle acceleration associated with the free stream velocity. Hence, the bottom shear stress is out of phase with the free stream velocity. With the analytical solution, by replacing u_ω with the formula of the solitary wave, the horizontal velocity profile and the bottom shear stress under a surface solitary wave can be calculated. Figure 1.2 shows an example of the time history of the normalized bed shear stress and free stream velocity, both quantities are normalized by the maximum

value of each, with τ_{bmax} = 2.15 kg/m-s^2 and U_{0m} = 0.36 m/s. The wave period in this case is set as 9.2 second, and Reynolds number is calculated as 2.0×10^5. Using Particle Imaging Velocimetry (PIV), Liu *et al*. 2007[26] measured the velocity field inside the bottom boundary layer under a surface solitary wave in a wave tank. The bottom shear stress was calculated as well from the velocity measurement. The experimental data was compared with the theoretical solution and good agreement was shown between these data. One of the significant findings is that the boundary layer flow changes its direction at a certain phase during the deceleration stage of the free stream velocity, which is always in the same direction of wave propagation in the case of solitary waves. The flow reversal is the result of unfavorable gradient during the flow deceleration stage. Consequently, the bed shear stress also changes the sign.

Define the Reynolds number as:

$$Re = \frac{aU_{0m}}{\nu} \tag{1.15}$$

where U_{0m} is the maximum free stream velocity, $2a$ the corresponding maximum fluid particle displacement, and ν the fluid viscosity. The order of magnitude of Reynolds number in the experiments performed by Liu *et al*. (2007)[26] is 10^4 and the boundary layer velocities remain laminar in all cases.

1.4 U-tube Experiment by Sumer *et al*. (2010)[21]

To investigate the evolution of boundary layer flows under a solitary wave for higher Reynolds number values, Sumer *et al*. (2010)[21] conducted a series of

experiments in an oscillating water tunnel and obtained the results of boundary layer flow with Reynolds number from 9.4×10^4 to 2.0×10^6. Their study was the following study of the investigation of wave boundary layers reported by Carstensen *et al*. (2010)[4]. Their experiments were carried out in a U-shaped water tunnel in which flows were driven by soliton-like pressure gradients in the direction of flows. One of the significant benefits applying the U-tube experiment is that we don't have to construct a large wave tank to perform a long wave. The pressure gradients were generated by a pneumatic system, with the piston of it was driven such that the free stream velocity and the pressure gradient in the tunnel would satisfy the equations of those under a solitary wave. The Reynolds number in their experiment is desinged from laminar region (Re $\leq 2.0\times 10^5$), to turbulent flow region (Re $\geq 2.0\times 10^6$).

In the laminar boundary layer flow region, Sumer *et al*. (2010)[21] showed that for a soliton-like pressure gradient their velocity measurements agreed very well with the theory by Liu & Orfila (2004)[24] and the wave tank measurements by Liu *et al*. (2007)[26]. The bed shear stress indeed changes sign due to the flow reversal during the deceleration stage of the free stream velocity, and leads over the free-stream velocity, which is in agreement with the oscillatory boundary layers (Fredsoe & Deigaard 1992)[9]. When the Reynolds number increased, for Re larger than 6.5×10^5 up to 2.0×10^6, they observed the appearance of single and multiple spikes in bed shear stress, produced by the passage of turbulent spots over the measurement location.

For the transition from laminar to turbulent boundary layer at $\mathrm{Re}_{critical} = 6.5\times 10^5$, the initial appearance of turbulent spots was seen in close relation to vortex tubes at $\omega\tau = 75\ ^\circ$, and the vortex tubes were able to influence the generation of

the turbuelnt spots. Two other important phases regarding turbuelnce generation were identified at $\omega\tau = 0^\circ \sim 30^\circ$, as the flow conditions regarding near bed flow velocity and pressure gradients were favorable for the initiation of turbulence during this period. When the turbuelnt spots emerged at these phases, the bed shear stress increased extensively. Flow visualization was provided for Re $= 2.7\times 10^5$, the results show that an array of vortex tubes was formed after near bed flow reversal. The vortex tubes nearby the tunnel bed have a 1cm vertical extent and a 1.5cm horizontal extent when fully developed. The wavelength of the tubes was around 2.5cm, which remained its shape with phase. Sumer *et al*. (2010)[21] reported that in the transient flow region, $2.0 \times 10^5 \leq \text{Re} \leq 5.0 \times 10^5$, such vortex tubes would formed by a shear layer instability. Once the vortex tubes were formed, the bed shear stress was significantly modified.

For a higher Reynolds number flow ($\text{Re} \geq 5.0 \times 10^5$), the 3-D turbulent structures were reported by Sumer *et al*. (2010)[21]. The appearance of single and multiple spikes in bed shear stress produced by the passage of the tubulent flow were observed, which indicates that with a higher Reynodls number flow, a 3-Dimensional analysis needs to be applied in order to fully understand and describe the turbulent flow. Liu (2006)[19] developed analytical solutions for the turbulent boundary layer flows under a solitary wave by applying Prandtl's law velocity profile and the eddy viscosity model. Liu (2006)[19] used the analytical solution to estimate the wave damping caused by the turbulent boundary layer. Regarding to the numerical analysis in the turbulent flow region, Vittori and Blondeaux (2008)[30] provided direct numerical simulation results for 3D turbulent boundary layer flows under a solitary wave. The discussion of the relation between the turbulent kinetic energy and the Reynolds stress on the wave amplitude was shown. It is of interests to note that, for the oscillatory bound-

ary layers, the role of the turbulent left from the previous half-cycle will trigger turbulence in the boundary layer, as demonstrated experimentally by Fredsoe *et al*. (2003)[10] and numerically by Costamagna *et al*. (2003)[5].

For an even higher Reynolds flow (Re $\geq 2.0 \times 10^6$), the 3-D spikes are expected to spread over the entire phase space, and the flow turns to be fully-developed turbulent, which is in agreement with the observation of oscillatory boundary layers (Jensen *et al*. 1989[14]; Lodahl *et al*. 1998[20] and Sumer *et al*. 2010[21]).

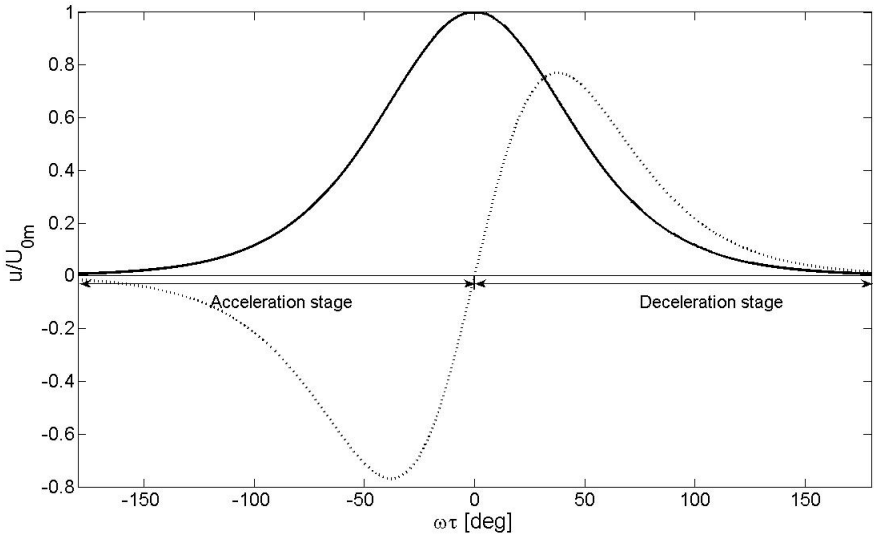

Figure 1.1: Sketches of the time history of the pressure gradient and the free stream velocity corresponding to a solitary wave.

1.5 Numierical comparison with Sumer's cases *et al*. (2010)[21]

The goal of this study is to conduct a numerical study based on Sumer *et al*. (2010)[21]'s designed cases. A 2-D spectral multidomain penalty method model is applied in this study to investigate the dynamics of wave-induced boundary

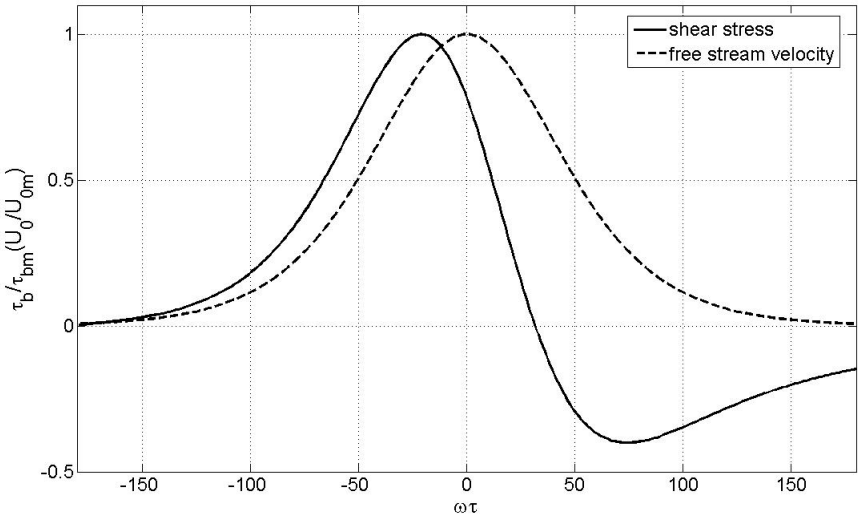

Figure 1.2: Sketches of the time history of the shear stress and the free stream velocity corresponding to a solitary wave.

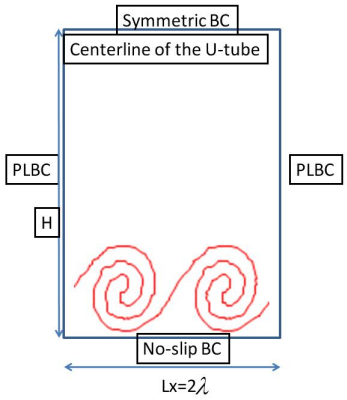

Figure 1.3: Sketches of the time history of the pressure gradient and the free stream velocity corresponding to a solitary wave.

layer under a propagating surface solitary wave using this developed direct numerical simulation code. There are several options conducting the simulation.

One option is to simulate it directly by constructing a wave-fixed frame, that is, by translating with a uniform speed C which equals to the wave speed but moves in the adverse direction. In this option the simulation domain is moving

with the whole solitary wave, which follows the idea of wave tank setup. However, this option has one critical problem. As the Spectral multidomain penalty method applied in this study requires the periodic lateral boundary condition to fulfill the Fourier spectral discretization condition, considering the trend of the shear stress curve, the shear stress might approximates to zero as phase reaches three wave period. Therefore, it might take at least three wavelengths to construct the horizontal computation domain. As the wave lengthes of the surface solitary waves in Sumer's experiments are all around 40m, the horizontal length of the simulation domain may be at least 120m. However, the size of the vortex tube is around 1cm, the simulation mesh should be refined to 1mm to be able to accurately simulate a vortex structure. Therefore, a large amount of grid points will be used in the simulation, but only with a small region that simulates the vortex tubes movement is needed. This will lead the computation inefficiency and difficulty.

Another choice is to simulate the temporal change of the boundary flow without considering the spatial change, which is the same idea as Sumer's experiment setup. In sumers experiments, the flow inside the U-tube, except near the ends, is uniform everywhere, which has a temporal change in both velocity and pressure gradient that is designed to be the same as a solitary wave passing. Such temporal change occurs everywhere at the same time without phase difference is not the same as the solitary wave movement in the wave tank. Each phase in the U-tube represents one temporal change of the solitary wave in the wave tank. In this setup, the simulation domain is now designed by simulating the instability, that is, the vortex tubes, rather than the entire solitary wave. The simulation therefore requires less grids and meshes, which makes the simulation more efficient.

In this study, the second option, the temporal change of the boundary flow, is applied. The flow will be driven by the solitary wave pressure gradient instead of the piston movement which is used in the experiment. The half height, rather than the whole height of the U-tube is simulated to reduce the computation load. A symmetreic boundary condition is applied in the upper boundary of the simulation domain. A sketch of the simulation setup is shown in figure 1.3. A detailed of the numerical setup will be discussed in a later chapter.

CHAPTER 2

THEORY

2.1 Instability Theory

2.1.1 A general description of the shear instability

This study focuses on the discussion of the shear instability in the wave boundary layer. As mentioned before, the movement of a solitary wave can be divided into the acceleration stage ($\omega\tau$=-180°~0°) and the deceleration stage ($\omega\tau$=0°~180°). The free stream velocity increases during the acceleration stage, reaches the maximum value when $\omega\tau$= 0°. After that the free stream velocity slows down and there is a flow reversal occurs near the boundary layer when negative velocity is generated due to the bottom shear stress. During the flow reversal, there is an inflection point where the horizontal velocity turns from positive to negative. Once the inflection point is formed, the flow has a potential to become unstable. The possibility of the occurance of the instability depends on the flow staus.

When the Reynolds number is big enough that the flow is no longer a laminar flow, the shear instability will take place, it will skew the profile of the wave from the direction of the basic flow and roll up the flow around the inflection point. The 2-Dimensional coherent structures of vortex tubes triggered by the shear instability will be formed.

With an even higher Reynolds number where the flow becomes turbulence, the instability keeps growing, a secondary three-dimensional Rayleigh-Taylor

instability will then be triggered in the cores of the billows, which causes small scales of disturbance in the lateral direction, and forms so-called 3-Dimensional turbulent spots, and the shear layer finally breaks up into turbulence.

In this study, the generation and evolution of the 2-Dimensional vortex structures are mainly discussed.

2.1.2 Stability Analysis

To explain the flow behavior, the transient flow with Reynolds number as 6.5×10^5 is applied. Some important parameters are listed in table 2.1. A horizontal velocity profile at $\omega\tau$=-90° is shown in figure 2.1. From figure 2.1, the horizontal velocity profile is positive moving down along the free stream direction, it goes to zero as the elevation is close to the bottom due to the visous effect. Figure 2.2 shows the horizontal profile while $\omega\tau$=45°, which is in the deceleration stage. From figure 2.2 we can see that the reverse flow occurs and there is an inflection point on the horizontal velocity profile. Around this inflection point, the horizontal velocity is positive above and negative below, therefore the vorticity can be generated and the shear layer will be rolled up.

The flow can be distinguished into a base state and a disturbance field. To define the disturbance field, the linearized theory is applied, and the method of normal modes is used, assuming that an arbitrary disturbance may be resolved into independent modes of the form[8],[29][17]:

$$(\eta, \phi) = (\hat{\zeta}, \hat{\phi})e^{i(kx+lz)+\omega t} \tag{2.1}$$

where η is the surface elevation, ϕ is the velocity potential. Properties marked with hat is the solution in each mode. k, l are the wave numbers of the instability in x- and z- direction, ω is the frequency. There are several approaches in stability analysis. In this study, the temporal theory is applied. In temporal theory, k is assumed to be constant, which allows ω to be complex. To further discuss the shear instability, first consider a vortex sheet in a homogeneous flow, the horizontal velocity profile can be depicted as shown in figure 2.3. Based on the dispersion relation:

$$(U_1 - c)^2 + (U_2 - c)^2 = 0 \tag{2.2}$$

where U_1 denotes the maximum horizontal velocity, U_2 is the minimum horizontal velocity as in figure 2.3. and the solution can be written as:

$$\omega = -\frac{1}{2}ik(U_1 + U_2) \pm \frac{1}{2}k(U_1 - U_2) \tag{2.3}$$

The phase velocity of the instability can be written as:

$$c = \frac{(U_1 + U_2)}{2}\frac{k}{\tilde{k}} \tag{2.4}$$

which is the average velocity of the basic flow that can be resolved in the direction of propagation, and $\tilde{k}$ is the total wave number composed by $\tilde{k}$= $(k^2 + l^2)^{1/2}$. The flow is always unstable as one of the modes grows exponentially, and the phase speed of the vortex tubes can determine the movement of the vortex tubes generated by the shear instability. If the phase speed is positive, the vortex

tubes will move to the right, and the vortex structures will move to the left once the phase speed turns negative.

To approximate our current problem into the vortex sheet problem, there are some assumptions needs to be addressed. Considering the snap shot of the horizontal velocity profile $\omega\tau$=45° in current problem as shown in figure 2.2, the flow is assumed to be in steady state. The other assumption is that the negative part of the horizontal velocity profile is approximated to remain constant as the vortex sheets problem. The horizontal velocity profile then can be approximated to the velocity profile from the vortex sheets problem as shown in figure 2.4. Within these two assumptions, the phase speed of current problem can also be represented by the averaged horizontal velocity.

Table 2.1: Parameters for the test case

U_{0m} (m/s)	ν (m^2/s)	ω (1/s)	T (s)
0.64	1.0×10^6	0.6756	9.3

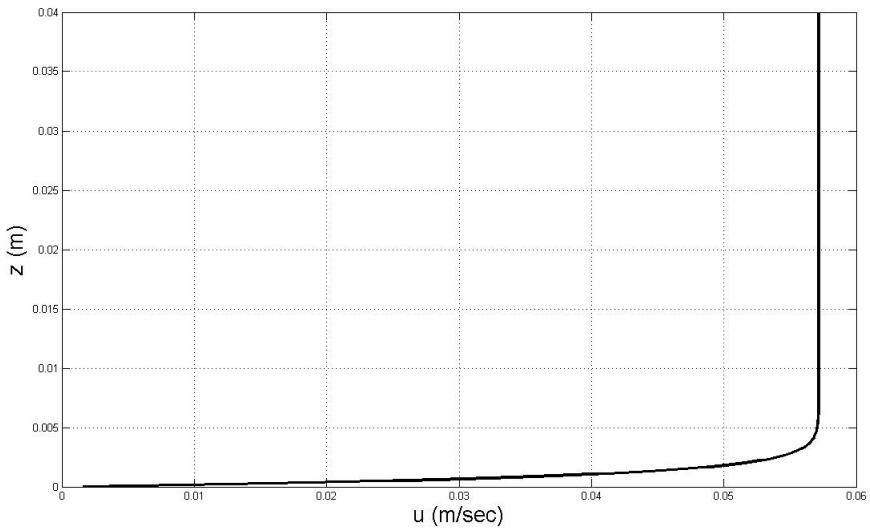

Figure 2.1: Horizontal velocity profile when $\omega\tau$ = -90 °

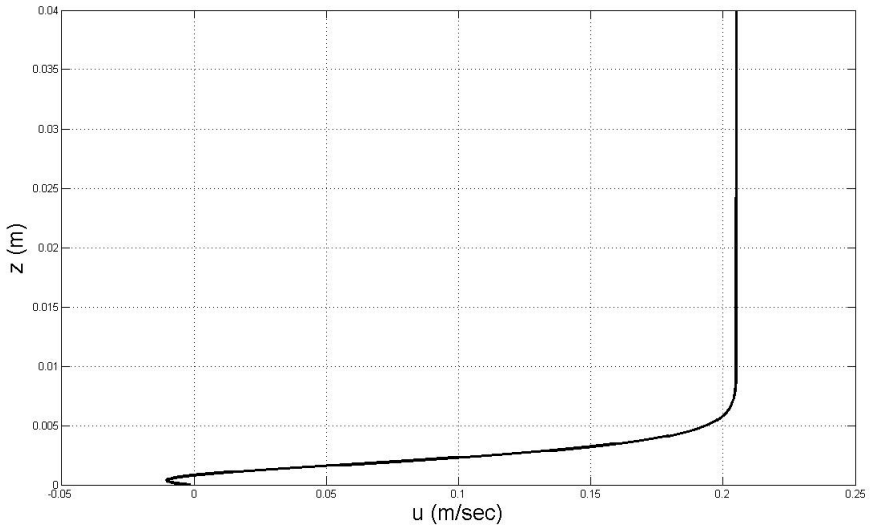

Figure 2.2: Horizontal velocity profile when $\omega\tau = 45$ °

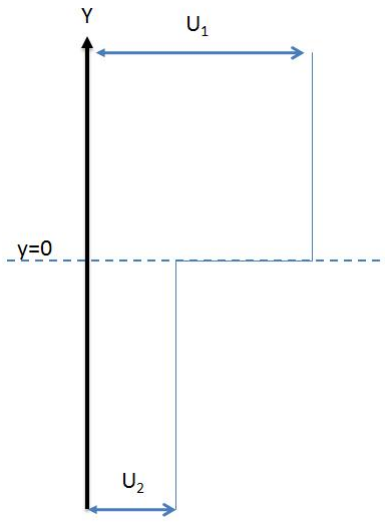

Figure 2.3: The generalized vortex sheet problem

2.1.3 Example

Within the instability theory discussed in previous section, the example with Reynolds number as 6.5×10^5 is taken as an example in this section. Figure 2.5 shows the time history of the vortex tubes velocity and the theoretical velocity

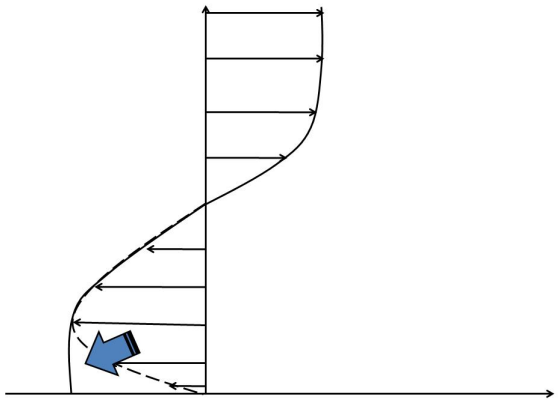

Figure 2.4: The horizontal velocity profile

of the shear instability (Phase speed of the instability). The vortex tubes velocity is calculated by applying the central difference scheme for the votex tubes movement. Figure 2.5 shows that the theoretical phase speed of the shear instability matches the vortex tubes velocity very well. Considering the vortex tubes movement which can be taken as the shear instability movement, the results indicate that the horizontal velocity of the vortex tubes is positive after the tubes are rolled-up, it starts to decrease after $\omega\tau \approx 90^\circ$, it becomes negative when $\omega\tau \approx 120^\circ$, which means that it moves to the opposite direction of the flow. The averaged phase speed after $\omega\tau$ =200° is 0.0372 m/s, where the average vortex tubes velocity after $\omega\tau$=200° is 0.0374 m/s, which indicates that the theoretical velocity of the shear instability can predict the vortex tubes movement very well.

2.2 Perturbation Velocity Field

In field or in the laboratory, the Kelven-Helmholtz instability is generated once the flow is no longer laminar, and the flow around the bottom boundary layer starts to reverse. However, in numerical simulation, the roll-up process will

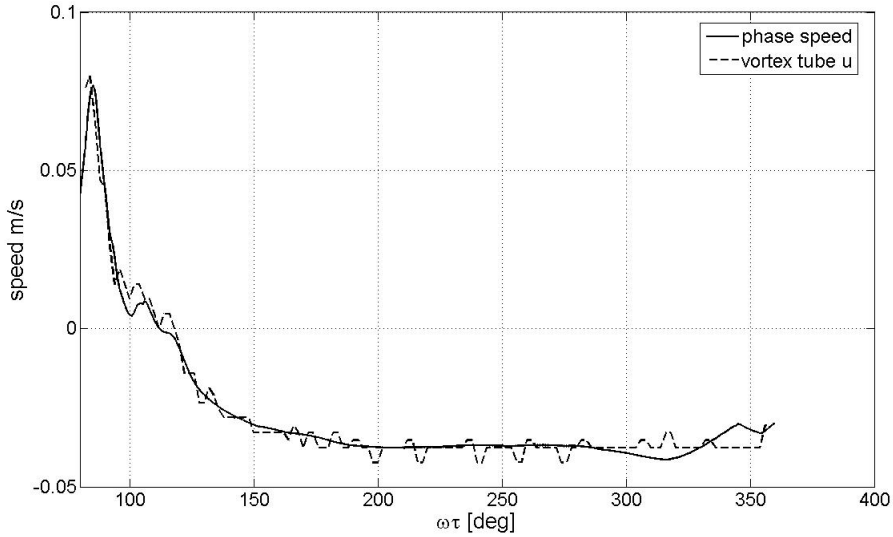

Figure 2.5: Time history of the vortex tubes velocity and compare it with the theoretical velocity of the shear instability (Phase speed of the instability), for Re = 6×10^5

not happen. This is because an disturbance needs to be applied to trigger the instability. In field or in the laboratory, there are many noises inside the flow field, the flow is not stable in real situation, so the instability can be generated. For the numerical simulation, an ideal environment is designed, there will be no noise inside the flow filed, therefore, there is a need to apply a perturbation velocity field to trigger the instability.

2.2.1 The design of the perturbation velocity field

Because of the unfavorable pressure gradient during the deceleration stage of the free stream flow, the flow reversal appears in the boundary layer flows. This phenomenon have been observed in Liu *et al.* (2007)[26] and Sumer *et al.* (2010)[21]. As the Reynolds number increases, the bounday layer thickness de-

creases and the shear strength increases. The Kevin-Helmholtz instability can be triggered by any small perturbation velocity field. To expedite the development of instability in our numerical simulations we introduce a perturbation velocity field designed to represent the flow structure of the most unstable primary and secondary instabilities in the boundary layer shear flows. Denoting $\hat{u}$ and $\hat{w}$ as the streamwise and vertical perturbation velocity component, the total velocities can be decomposed into:

$$u(x, z, t) = \tilde{u}(x, z, t) + a\delta(\omega\tau)\hat{u}(x, z) \tag{2.5}$$

$$w(x, z, t) = \tilde{w}(x, z, t) + a\delta(\omega\tau)\hat{w}(x, z) \tag{2.6}$$

where a is a constant parameter controlling the amplitude of the velocity perturbation and $\delta()$ denotes the delta function. To trigger the Kevin-Helmholz instability efficiently, the preturbation velocity field is inserted into the velocity field at the phase $\omega\tau = 0^\circ$ for only one time, when the free stream velocity reaches its maximum value and the pressure gradient starts to reverse its direction. Following Smyth and Moum (2000)[28], the perturbation velocity field used in this study is:

$$\hat{u}(x, z, t) = \frac{u_0}{2k_0}(-\cos\frac{2k_0x}{h_0} + 2b\cos\frac{k_0x}{h_0})\tanh\frac{2(z - z_0)}{h_0}\text{sech}^2(\frac{2(z - z_0)}{h_0}) \tag{2.7}$$

$$\hat{w}(x, z, t) = \frac{u_0}{4}(\sin\frac{2k_0x}{h_0} - b\sin\frac{k_0x}{h_0})\text{sech}^2(\frac{2(z - z_0)}{h_0}) \tag{2.8}$$

where b is the relative strength of the primary instability in the vortex pairing instability (Winant and Brownand 1974)[31], h_0 characterizes the shear layer thickness, u_0 the characteristic velocity, k_0, normalized by h_0, the streamwise wave number of the fastest growing eigen mode of a parallel flow, and z_0 the position of the centerline of the shear layer. Noted that the perturbation velocity components, ($\hat{u}$,$\hat{w}$), satisfy the continuity equation. A typical vertical profile of the horizontal perturbation velocity component is shown in figure 2.6. Figure 2.6 indicates the shape of the perturbation velocity filed is similar to the horizontal velocity filed, which is positive beyond the inflection point and negative below the inflection point. This is the reason the (tanh()sech^2()) equation is chosen.

The parameters appearing in the perturbation velocity field need to be selected carefully so that while the flow instability is triggered, only minimum numerical oscillations are created. Among the six parameters appearing in the equations defining the perturbation velocity field, the maximum free stream velocity, U_{0m}, is assigned as the characteristic velocity, u_0. The magnitude parameter a is specified as a = 0.001, ensuring that the simulations approximate the growth of infinitesimal perturbations. The parameter b in perturbation velocity field specifies the ratio between the first and second modes in terms of k_0 and takes the values of b = 0.4177. This choice indicates that the subharmonic mode will be added with one-half the kinetic energy of the primary (Smyth *et al*. 2000)[28]. The remaining 3 parameters, the half thickness of perturbation layer h_0, the streamwise wave number of the fastest-growing eigenmode k_0, and height of the center of the perturbation layer z_0, are determined according to the properties of the shear flow layer. These parameters are related to the shear layer thickness, δ_ω, as follows:

$$h_0 = \frac{\delta_\omega}{3}, z_0 = \frac{2\delta_\omega}{3}, k_0 = \frac{2\pi h_0}{\lambda} \tag{2.9}$$

A typical shear layer profile in the solitary wave boundary layer is shown in figure 2.7 during the flow reversal. The shear layer thickness, δ_ω, is defined as:

$$\delta_\omega(\omega\tau) \equiv \frac{u_{max} - u_{min}}{(du/dz)_{max}} \tag{2.10}$$

where u_{max} is the maximum value of the streamwise velocity and u_{min} is the coreesponding minimum value. With the same vertical velocity profile, the momentum thickness of the shear layer can be determined by:

$$\delta_m = \int_{z(u_{min})}^{\infty} \frac{u - u_{min}}{u_{max} - u_{min}} (1 - \frac{u - u_{min}}{u_{max} - u_{min}})\, dz \tag{2.11}$$

And it is found that after the integration,

$$\delta_m = \frac{\delta_\omega}{4} \tag{2.12}$$

In the shear layer flow, the Strouhal-number $S_t = 0.032$ corresponds to the natural frequency, f, of the shear layer and it can be expressed as,

$$S_t = \frac{f\delta_m}{\bar{u}_{vortex}} = 0.032 \tag{2.13}$$

where $\bar{u}_{vortex}$ is the convective velocity of vortex tube, which is calculated by averaging the maximum and minimum velocity,

$$\bar{u}_{vortex} = \frac{(u_{max} + u_{min})}{2} \tag{2.14}$$

Then the wavelength of the vortices in a shear layer, λ, i.e., the span between vortex tubes, is estimated by (Batchelor *et al*. 2000 [1]):

$$\lambda = \frac{\bar{u}_{vortex}}{f} = \frac{\delta_m}{0.032} \tag{2.15}$$

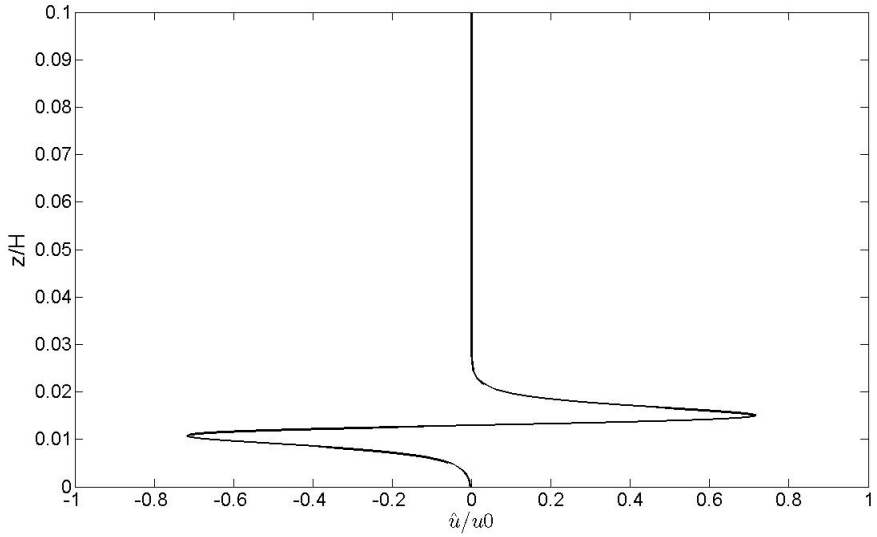

Figure 2.6: A sketch of the vertical profile of the perturbation velocity at $\frac{k_0 x}{h_0}=\frac{\pi}{2}$ with the following parameter values: h_0 = 0.1mm, z_0 = 0.22mm, k_0 = 0.268.

To determine the value of vorticity thickness that is used to calculate the parameters of the perturbation velocity field, the vorticity thickness when the Kevin-Helmholz instability is about to occur is used. In this study, the average time of the phase when the bottom shear stress goes to negative, and the phase when the adverse pressure gradient reaches maximum value is calculated and the vorticity thickness at this phase is applied. The first phase shown above, that

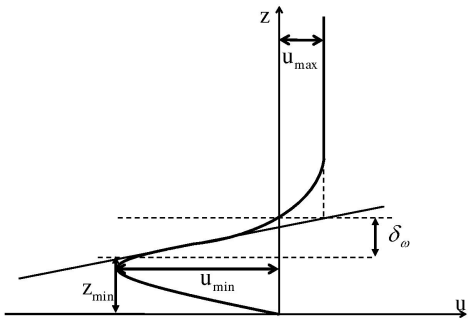

Figure 2.7: A sketch of the velocity profile duirng the flow reversal phase, which indicates the definition for a shear layer thickness in the sollitary wave boundary layer

is, after the bottom shear stress goes to negative, indicates that the flow begins to reverse and the shear layer begins to form. The second phase, when the adverse pressure gradient reaches the maximum values, represents the last chance of transition. Inside this range the Kevin-Helmholz instability is essential to be triggered. Therefore, an average value is chosen to be the phase δ_ω when the vorticity thickness is selected.

2.3 Numerical Model

2.3.1 Govening Equation

In this study, the 2-D Navier-stokes equations are used as the governing equations for the numerical model:

$$\nabla \cdot u = 0, \tag{2.16}$$

$$\frac{\partial u}{\partial t} = -\frac{1}{2}[u \cdot \nabla u + \nabla(u \cdot u)] - \frac{1}{\rho} \nabla p + \nu \nabla^2 u, \tag{2.17}$$

where u is the velocity vector, t the time, ρ the density, p the pressure, and ν the kinetic viscosity (1.0×10^{-6} m^2/s for water). In terms of the Cartesian coordinate system (x,z), the x-axis is pointing in the streamwise direction. The velocity vector has two components, u = (u,w), and the gradient vector can be written as $\nabla = (\partial/\partial x, \partial/\partial z)$.

With the governing equations and initial, boundary conditions, the time series of free stream velocity and the corresponding pressure gradient can be computed. Noticed that while simulating the flow in the solitary wave bounday layer following the U-tube experiments designed by Sumer *et al*. (2010)[21], the pressure gradient is $\partial p_0/\partial x$, which is a function of time only and drives the free-stream velocity. Moreover, it is not appropriate to specify the velocity on the boundaries since the velocity profile along the vertical direction is not uniform because of the effect of the tunnel bed. The magnitudes of pressure at the left and right boundary do not equal to each other although they have a constant vertical distribution, which will violate the periodical condition if the pressure is specified at boundaries.

To solve this problem, introducing $\acute{p}$ as the pressure due to the adjustment necessary for the boundary layer flow. The pressure gradient term appearing in equation (2.17) then can be written as:

$$\frac{1}{\rho} \bigtriangledown p = \frac{1}{\rho} \bigtriangledown p_0 + \frac{1}{\rho} \bigtriangledown \acute{p} \tag{2.18}$$

The pressure gradient corresponding to the free stream velocity field acts on the fluid particle similar to a volume force which is constant throughout the whole computational domain and can be calculated using equation (1.12). Thus, the unknowns to be solved are the total velocity (u,w) and the pressure p in equation (2.16) to (2.18).

2.3.2 Computational domain, Initial and boundary conditions

The computational domain is rectangular with dimensions $L_x \times \frac{H}{2}$, representing a subregion of the U-tube, which covers one-half of the U-tube heighet, H, from the bottom to the centerline of the U-tube, and a predetermined length, L_x, that is sentive in every single case, in the stream-wise direction. In the U-tube experiments the free-stream velocity is uniform at each elevation and the velocity and pressure are periodic in the streamwise direction. Therefore the periodic lateral boundary condition is applied:

$$(u, w, \acute{p})(x, z, t) = (u, w, \acute{p})(x + L_x, z, t) \tag{2.19}$$

The use of periodic lateral boundary condition requires that the length of the domain is the multi-fold of the wavelenth of the K-H shear instability. In this study, two vortex tubes are simulated in each case, that is, we define $L_x = 2 \times \lambda$, where λ is the wavelength of the K-H instability.

The symmetric condition is applied along the upper boundary, which is the

centerline of the U-tube flow, therefore the top boundary is a free-slip nondeformable surface:

$$\frac{\partial u}{\partial z} = 0, \quad w(x, \frac{H}{2}, t) = 0, \quad on \;\; z = H \tag{2.20}$$

The bottom boundary is assumed to be a solid wall with no-slip boundary condition:

$$u = w = 0, \quad on \;\; z = 0 \tag{2.21}$$

The simulation starts from a still state when velocities and pressure are all zero throughout the entire simulation domain. The initial condition of the model is specified as:

$$u(x, z, 0) = w(x, z, 0) = \acute{p}(x, z, 0) = 0 \tag{2.22}$$

2.3.3 Numerical Implementation

The governing equations are implemented by a 2-D spectral multidomain penalty method model developed by Diamessis *et al*. (2005)[23]. The spectral method is recently widely applied to the numerical analysis of boundary layer flow. Diamessis & Redekopp (2006)[7] presented the examination of the boundary layer flows under internal waves, the pseudo-spectral method was applied. The temporal discretization of the model ensures maximum temporal accuracy by combining third order stiffly stable and backward differentiation schemes with a high-order boundary condition for the pressure. A high-accuracy pres-

sure projection scheme is employed for the temporal discretization of equation (2.16) and (2.17), which contains three fractional steps: the explicity treatment of the non-linear terms, the implicit solution of a Poisson equation for the pseudo-pressure, which ensures an incompressible velocity field, and the implicit solution of a Helmholz equation for the viscous term, where the physical boundary conditions are imposed. The third order backward differentiation scheme is used to discretized the temporal derivative. The non-linear terms are advanced in time via a third order stiffly stable scheme allowing for maximum value of a stable timestep. The above splitting scheme was proved by Guermond and Shen (2003)[12] to be equivalent to the rotational form of a velocity-correction projection scheme whose second order variant exhibits $O(\triangle t^2)$ accuracy in both u and ϕ.

For the spatial discretization of the numerical model, as it is periodic in the horizontal domain, and non-periodic in the vertical direction, different treatments are applied in this study. In the stream-wise periodic direction, the Fourier spectral discretization is used with N_x Fourier modes in the longitudinal direction. Horizontal derivatives are calculated in a straightforward fashion in Fourier spectral space. In the non-periodic vertical direction, a spectral multi-domain discretization is used. The computational domain is partitioned into M subdomains. Within each subdomain, Legendre spectral discretization is used[2][3]. The height H_k (k = 1,..., M) in each subdomain can be freely specified. The order of approximation N_k is fixed and equal to a fixed vale N in all subdomain. In each subdomain, any function $f(z)$ is aprroximated on the Gauss-Legendre-Lobatto grid. Specral multidomain methods are designed as collocation methods and in this study the considered function $f(z)$ is approximated in nodal, but not modal form. Subdomains communicate with their neighbors via

a simple patching condition (Diamessis *et al*. 2005[23]). As this study focuses on the boundary layer flow, which is only a small part compared with the entire flow domain, the multi-domain scheme can resolve the bottom boundary layer with enough accuracy and meanwhile resolve adequately the free-stream dominated ambient, which ensures the efficiency for the under-resolved simulations at high Reynolds numbers.

The stability for under-resolved simulation at high Reynolds number flows is ensured through the use of the penalty method and the spectral filtering. The penalty method is implemented in different formulations for both the explicit non-linear term advancement and the implicit treatment of the viscous terms. It consists of collocating a linear combination of the equation and bounday/patching conditions (the latter multiplied by a penalty coefficient) at the boundaries and sub-domain interface, respectively. The computation thus becomes more stable as the penalty methods provide a smooth transition from the subdomain interface to the interior of the subdomain while dealing with high Re internal dynamics of the flow without having to resolve the thin numerical visous physical boundary layers or internal sharp gradients at sub-domain interfaces (Diamessis *et al*. 2005[23]).

In this study, the p-th order low-pass spectral filter on the numerical solutioin is applied, as while the penalty method allows an increase of the value of the Reynolds number by roughly two order of magnitude, which cause the numerical stability issue while dealing with high-Reynolds-number flow. In this study, an exponential filter is used[11]:

$$\sigma(k) = 1, 0 \leq k \leq k_c \sigma(k) = exp[-\alpha(\frac{k - k_c}{N - k_c})^p], k_c \leq k \leq N \tag{2.23}$$

where p is the filter order, k_c the filter lag, and α = - ln ϵ_M with ϵ_M the machine

precision. The filtered solution f^F now can be expressed in terms of the modes of the numerical solution as:

$$f^F(z_i) = \sum_{j=0}^{N_{k-1}} \sigma(k_j) \tilde{f}_j P_j(z_j) \tag{2.24}$$

where k_j is the jth discrete Legendre mode. An analogous expression may be written for filtering in Fourier space.

2.4 Rules to Analyze Vortex Coherent Structures

The main purpose of this study is to look at the Kevin-Helmholz instability in the bottom boundary layer generated by the surface solitary waves. It is therefore important to analyze the vortex coherent structures created by the shear instability. In our numerical study, the length of the horizontal domain, L_x, is set to be twice of the wavelength of the vortices in a shear layer, λ for each case, that is, $L_x = 2\ \lambda$. Therefore, in the numerical simulation, two vortex tubes will be observed once the instability theory is triggered. In this study, to measure the vortex structures, some rules are made to analyze the vortex coherent structures.

2.4.1 The contour of the vortex tubes

To analyze the movement of the vortex tubes, first the rescaled vortex contour with different phase is being plotted. The vortex tubes will appear some time after the perturbation velocity field is being inserted, the vortex tubes will then start to move upward and based on the instability they will move along with the free stream flow or against the flow. A general description of the vortex tubes

movement will be addressed. The vortex tubes will detach from the bottom shear layer, the observation time of detachment will be recorded within each case.

2.4.2 The maximum vorticity of the vortex tubes

There are several methods to analyze the vortex structures, this study looks at the evolution of the maximum vorticity in single vortex tube, to represent the behavior of the vortex structure. Within each case, the left vortex tube is selected. The maximum vorticity of the vortex tube is calculated, the time history of the magnitude of the maximum vortictiy is recorded, to represent the strength of the vortex tube. The time line in each case has been transferred to the angular unit, the time frame is from -180° to 360°. The time history of the horizontal and vertical movement of the maximum vorticity in each case are recorded to describe the movement of the vortex tubes.

2.4.3 The vorticity flux study

To study the sediment transport, it will be interesting to look at the time history of the vorticity flux being transported. By assuming the vorticity is a passive scalar, the vorticity flux can be taken as the mass flux, which therefore can give a preliminary estimation of the sediment transport by the vorticity.

CHAPTER 3

COHERENT STRUCTURES IN SURFACE SOLITARY WAVE BOUNDARY LAYER

3.1 Cases description

To study the structure of the 2D vortex tubes, case5 ~ 10 from Sumer *et al*. (2010)[21] are taken and reproduced by the numerical model (Diamesis *et al*. 2005[23]) in this study. The Reynolds numbers of these cases are lying in the transition regime where the boundary layer flow experiences vortex tubes. A summary of wave parameters, grid resolution, and spectral filter orders considered in each numerical simulation case is provided in table 3.1. Where T=$2\pi/\omega$ is the governing parameter of flow motions, and can be taken as the characteristic time scale. U_{om} represents the maximum free stream velocity, ω is the angular frequency, ν is the kinematic viscosity of water, Re_s is the Reynolds number obtained from Sumer *et al*. (2010)[21], which can be calculated by aU_{om}^2/ν . Re_c is the Reynolds number calculated by $U_{om}^2/\omega\nu$ in this study. Noticed that a, the half of the stroke of the water particle displacement in the free stream region, is calculated by U_{om}/ω in this study, where in Sumer *et al*. (2010)[21], a is found by measuring,therefore there is slightly difference in the values of the Reynolds number between the current study and Sumer *et al*. (2010)[21] for each case. δ_ω is the vorticity thickness of shear layer, and λ is the wavelength of Kevin-Helmholtz instabilities.

The total numerical simulation duration for each of the six cases is 1.5 of the wave period. We define the start of the simulation as $\omega\tau$=-180° , the simulation ends up when $\omega\tau$=360°. More, the numerical simulation for each case can be

divided into two parts. For the first part the simulation without inserting the perturbation velocity field is performed, to exam the hydrodynamic properties such as vorticity thickness, bed shear stress, and horizontal velocity profile, in order to design the perturbation velocity field. In the second part, the perturbation velocity field is inserted into the water column when the flow reaches maximum free stream velocity, to trigger the shear instability. The results of the bed shear stress and the horizontal velocity profile from the first part, where no perturbation velocity field is introduced into the simulation, are performed. The structures and the evolutions of the vortex tubes that represent the strength and magnitude of the shear instability are shown as the second part of the results.

Table 3.1: Summary of simulation conditions

case	T (s)	U_{0m} (m/s)	ω (m/s)	ν (m^2/s)	Re_c	Re_s	δ_ω (mm)	λ (cm)
1	9.2	0.36	0.683	1.E-06	1.90E05	2.0E05	2.807	2.195
2	9.3	0.41	0.676	1.E-06	2.49E05	2.7E05	2.824	2.205
3	8.9	0.45	0.706	1.E-06	2.87E05	3.1E05	2.762	2.160
4	9.4	0.53	0.668	1.E-06	4.20E05	4.4E05	2.839	2.220
5	9.0	0.56	0.698	1.E-06	4.49E05	4.8E05	2.778	2.170
6	9.3	0.64	0.676	1.E-06	6.06E05	6.5E05	2.824	2.205

3.2 Grid independent test

Before the cases simulation, it is important to obtain a set of grid that is suitable and can produce stable solutions for each case. To reach this point, different resolutions of the grid setup have to be designed and the grid independent test is conducted. A suitable setup of the grid can be obtained once a finer resolution

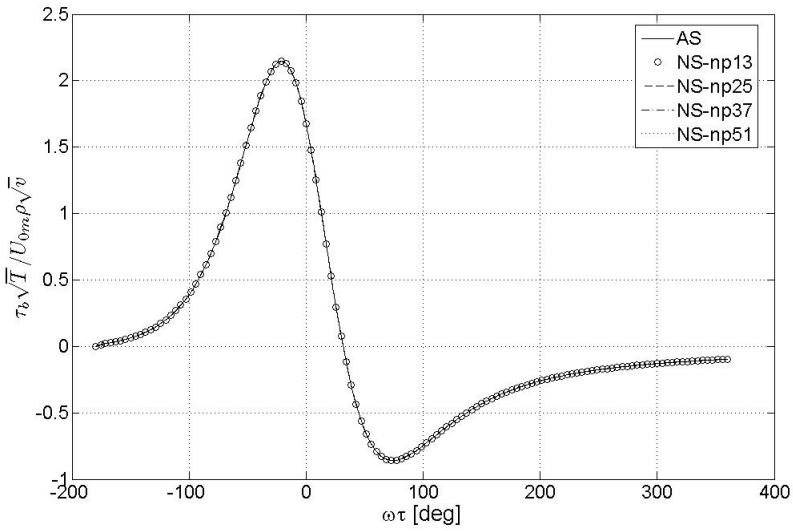

Figure 3.1: Time history of the rescaled bed shear stress for Re = 5.9×10^4 without perturbation velocity field in different grid resolution

of grid makes no difference on simulation. To perform the grid independent test, case2, 5, 12 from Sumer *et al*. (2010)[21] are chosen to check the model's validity and adaptability. These three cases represent the case for laminar flow regime, the transition with vortex tubes generation, and the transition to turbulent regime, respectively. Table 3.2 shows a summary of the simulation conditions for these three cases. 4 sets of grid points in the vertical sub-domain are designed. The mesh sets for the grid independent test are shown in table 3.3, where N_x is the amount of the grid points along x-direction,which is set to be 96 for all cases. As shown in table 3.2, that the length of the horizontal domain are all around 4.2cm, 96 mesh points are found to be efficient and precise enough for this study. M is the number of sub-domain, and is set to be 11 for all cases. More points in one vertical sub-domain means more resolution being inserted into the simulation. Points starting from 13 to 51 are increasing case by case by a factor of 2 in order to see the computation difference of number of grid point

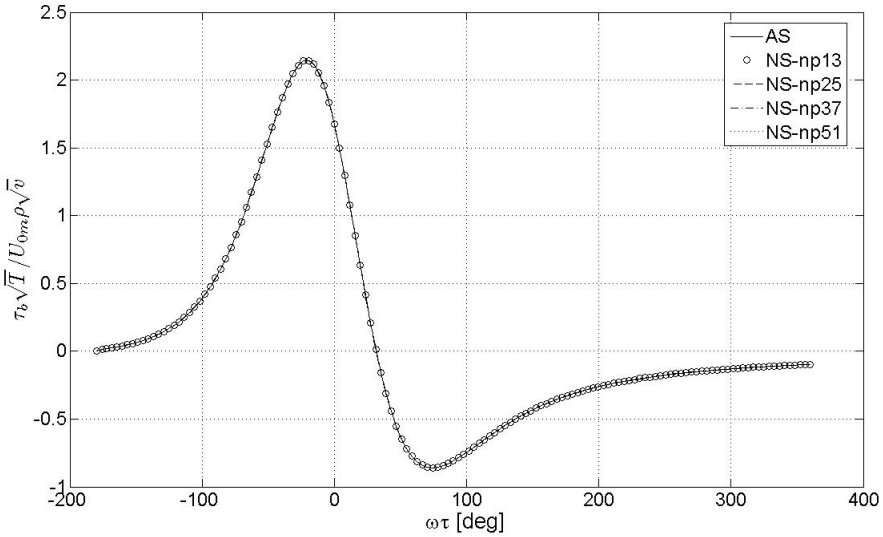

Figure 3.2: Time history of the rescaled bed shear stress for Re = 2.0×10^5 without perturbation velocity field in different grid resolution

inside each sub-domain. In all the simulations in this study, the thickness of the subdomain from the bottom to the top are 0.01cm, 0.02cm, 0.04cm, 0.08cm, 0.16cm, 0.32cm, 0.64 cm, 1.28cm, 2.56cm, 5.12cm, and 4.27cm. Two sets of simulations are done, the first test phase is run without inserting the perturbation velocity field, the second test phase is run with the perturbation velocity field. Time history of the rescaled bed shear stress for each case in both test phases are shown from figure 3.1 to figure 3.6.

The results show that for the first test phase, the bed shear stress matches quite well for all the three Reynolds number cases using 4 different mesh resolutions, as can be seen from figure 3.1 to figure 3.3. For the second test phase, the results show that for case 2, the laminar flow case, nodal point 13 case has little difference within the end of the simulation. For case5, all 4 cases remain the same when the flow is stable, then np13 case has visible difference around largest negative bed shear stress at $\omega\tau \approx 110\,^\circ$, the other 3 cases remain the same

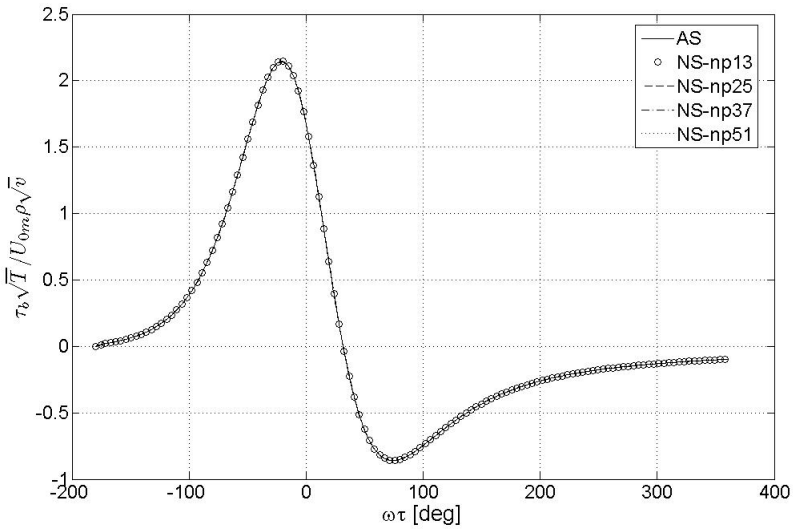

Figure 3.3: Time history of the rescaled bed shear stress for Re = 1.22×10^6 without perturbation velocity field in different grid resolution

in all simulation time. For case 12, all 4 cases remain same when the flow is stable, then np13 case has visible difference after largest negative bed shear stress, results from the other 3 cases remain the same in all simulation time. As this study focuses on the transition with vortex tubes generation regime, the case where 25 nodal points are inserted into one sub-domain is then proved to be the most suitable grid set, and is taken as the simulation grid setup in this study.

Table 3.2: Summary of Test case 2, 5, 12 from Sumer *et al*. (2010)[21]

case	T (s)	U_{0m} (m/s)	ω (m/s)	ν (m^2/s)	Re	δ_ω (mm)	λ (cm)	$L_x(cm)$
2	8.4	0.21	0.748	1.E-06	5.90E04	2.68	2.10	4.20
5	9.2	0.36	0.683	1.E-06	2.00E05	2.81	2.19	4.38
12	8.3	0.96	0.757	1.E-06	1.22E06	2.86	2.08	4.16

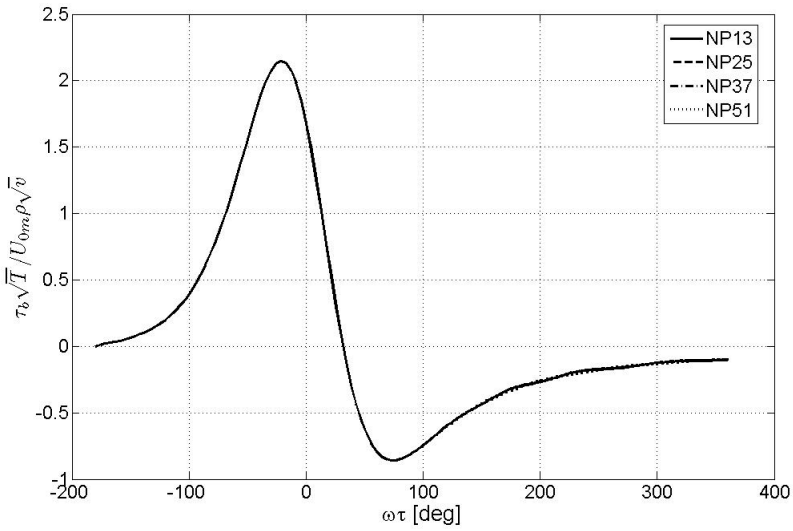

Figure 3.4: Time history of the rescaled bed shear stress for Re = 5.9×10^4 with perturbation velocity field in different grid resolution

Table 3.3: The mesh sets for the grid independent test

Name	N_x	M	N
mesh1	96	11	13
mesh2	96	11	25
mesh3	96	11	37
mesh4	96	11	51

3.3 Results

3.3.1 Laminar flow at low Reynolds numer

In the low Reynolds number flow, where Re < 2.0×10^5, the flow remains laminar as the surface solitary wave comes by. Vortex structure will not appear even the perturbation velocity field is correctly inserted. Figure 3.7 depicts the

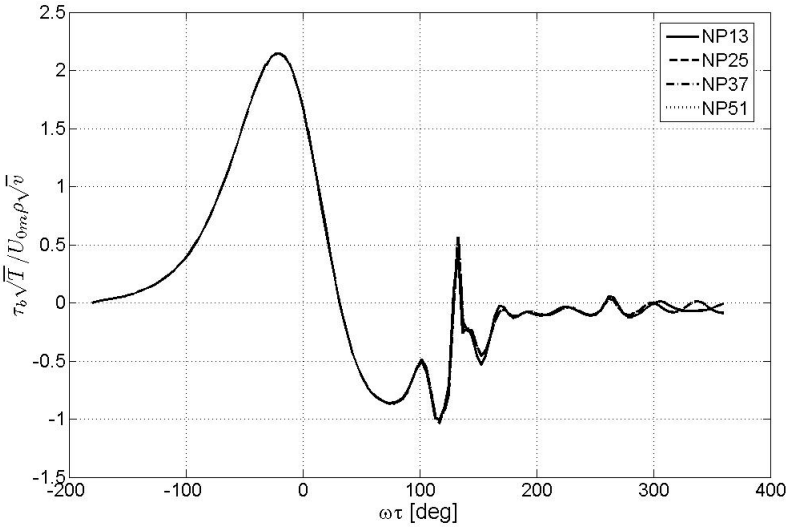

Figure 3.5: Time history of the rescaled bed shear stress for Re = 2.0×10^5 with perturbation velocity field in different grid resolution

phase variation of the bed shear stress done by the numerical simulation for Re = 5.9×10^4, which is compared with the analytical solution provided by Liu & Orfila (2004)[24], to show that the perturbation velocity field does not trigger the instability for low Reynolds number flow. Noticed that for the numerical analysis in this case, the perturbation velocity field is inserted to trigger the K-H shear instability, due to the low Reynolds number, the laminar flow remains stable for the simulation without the appearance of the vortex tubes, therefore, theoretically, the numerical results should be very close to the analytical solution. In figure 3.7, there is no observable difference between the numerical results and the analytical solution. And there is no vibration of the bed shear stress considering that if the vortex tubes are generated there will be vibration of bed shear stress. This shows that the shear instability does not occur at this low Reynolds number flow. Notice that there is nearly perfect match for these two analysis results. This is because that the analytical solution is derived by neglecting the

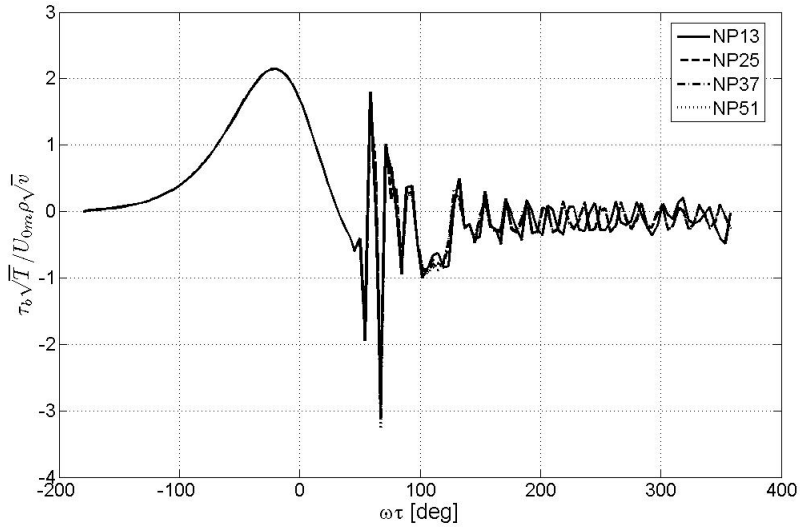

Figure 3.6: Time history of the rescaled bed shear stress for Re = 1.22×10^6 with perturbation velocity field in different grid resolution

nonlinear inertial term in the boundary layer momentum equation, where in the numerical simulation of the U-tube experiment, the same equation is essentially formed and solved.

3.3.2 Transitional flow at intermediate Reynolds number

As the Reynolds number increases, the flow tends to be unstable, the vortex tubes made by the shear instability will be generated in this transitional flow. Figure 3.8 compares the numerical results of the phase variation of the bed shear stress with the experiemntal data for the transitional flow at Re = 4.4 ×10^5. Noted that in the U-tube experiments Sumer *et al*. (2010)[21] repeated 30 times for the same Reynolds number flow condition. In this study, 2 experimental data sets are presented and compared with the numerical results as shown in figure 3.8. Figure 3.8 shows that there is some difference between these 2 ex-

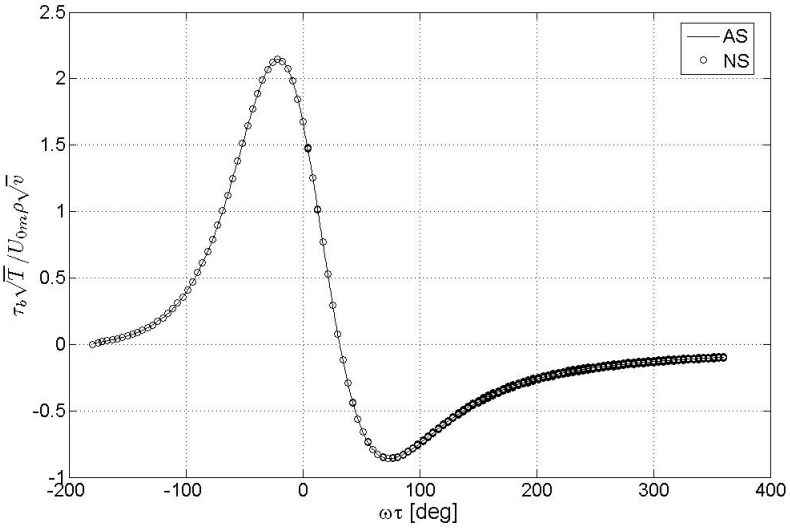

Figure 3.7: Phase variations of the bed shear stress for the laminar flows at Re = 5.9×10^4. The solid line is the analytical solution done by Liu & Orfila (2004)[24], while the circles represent results from the numerical analysis

periment data sets after the vortex tubes are genereated; however, the general features of these data remain similar. Figure 3.8 also shows that the numerical results and the experimental data fit very well, the oscilation of the bed shear stress occurs around $\omega\tau\approx50°$.

In the transitional flow region where vortex tubes are generated, it will be interesting to look at the phase variation of the bed shear stress along the horiztontal plane, which can give us an idea of how bed shear stress evolves with time along the horizontal plane. Figure 3.9 displays the normalized bed shear stress in the x-τ plane for the transitional flows cases 1, 4, and 6, that is, at Re = 2.0×10^5 (left), 4.4×10^5 (middle), and 6.5×10^5 (right), respectively. The horizontal domain x was normalized by $2a = \frac{2U_{0m}T}{2\pi}$. From figure 3.9 the phase at which the bed shear stress is no longer uniform in the stream wise direction can be identified, which can be taken as the incipient of the shear instability. Figure 3.9

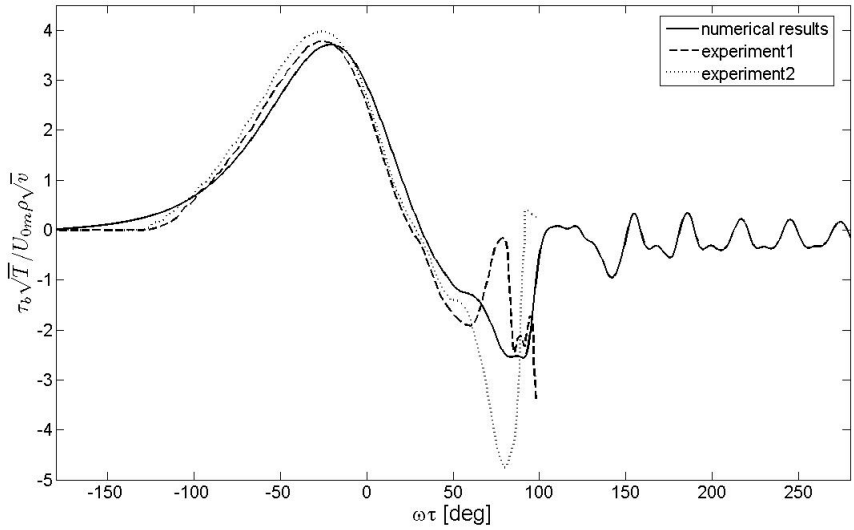

Figure 3.8: Phase variations of the bed shear stress for the laminar flows at Re = 2.0×10^5. The solid line is made by the numerical analysis, while the dash line is the analytical solution done by Liu & Orfila (2004)[24]

shows that for higher Reynolds number flows the incipient phase occurs earlier because of a stronger flow condition.

Once the vortex tubes are generated, it is interesting to trace the tubes, to understand under what flow conditions (what Reynolds number) will the vortex tubes be generated and how the vortex tubes are moving under such flow condition. For lower Reynolds number flow in the transitional flow region (Re around 2.0×10^5), the vortex tubes will move directly opposite to the flow direction, that is, to the left of the domain. For a higher Reynolds number flow (Re around 5.0×10^5), the vortex tubes will first follow the flow direction to the right direction. These vortex tubes do not move very far downstream before they start to move to the opposite direction. As an example, figure 3.10 and figure 3.11 display six phase frames for describing the shape and the movement of the vortex tubes for Re = 6.5×10^5, the time frame in figure 3.10 and figure 3.11 is

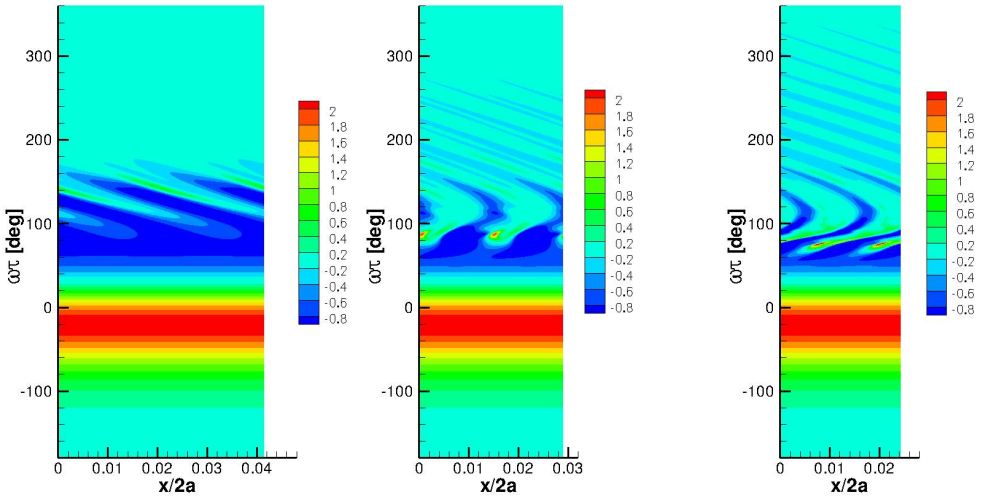

Figure 3.9: Normalized bed shear stress in the x-τ plane at Re = 2.0×10^5(left), 4.4×10^5(middle), 6.5×10^5(right)

from $\omega\tau$ = 82° ~ 180°, and the spatial domain is normalized by $2a$. Figure 3.10 and figure 3.11 show that the vortex tubes detach from the bottom boundary layer at $\omega\tau$ = 82°, and start to move along the flow direction to the right of the domain, as shown in the upper right panel at $\omega\tau$ = 90° in figure 3.10. Then the vortex tubes begin to move to the left of the domain. the lower panel in figure 3.10 and the upper left panel in figure 3.11 show that at $\omega\tau$ around 120°, the vortex tubes seem to move in a relative stable status to the left of the domain, the size and shape of the tubes remains during these periods. The remaining 2 panels in figure 3.11 show that after a short time when the whole simulation duration lasts for one wave period, the effect from the surface solitary wave is nearly gone, the vortex tubes continue moving to the left. Noticed that at $\omega\tau$ = 134°, tube A is reaching the left boundary. Due to the symmetric lateral boundary condition tube A and B will re-enter the domain. The later shape and movement of vortex tubes then can be observed following the simulation. From the later 2 panels in figure 3.11 we can find that the shape of the vortex

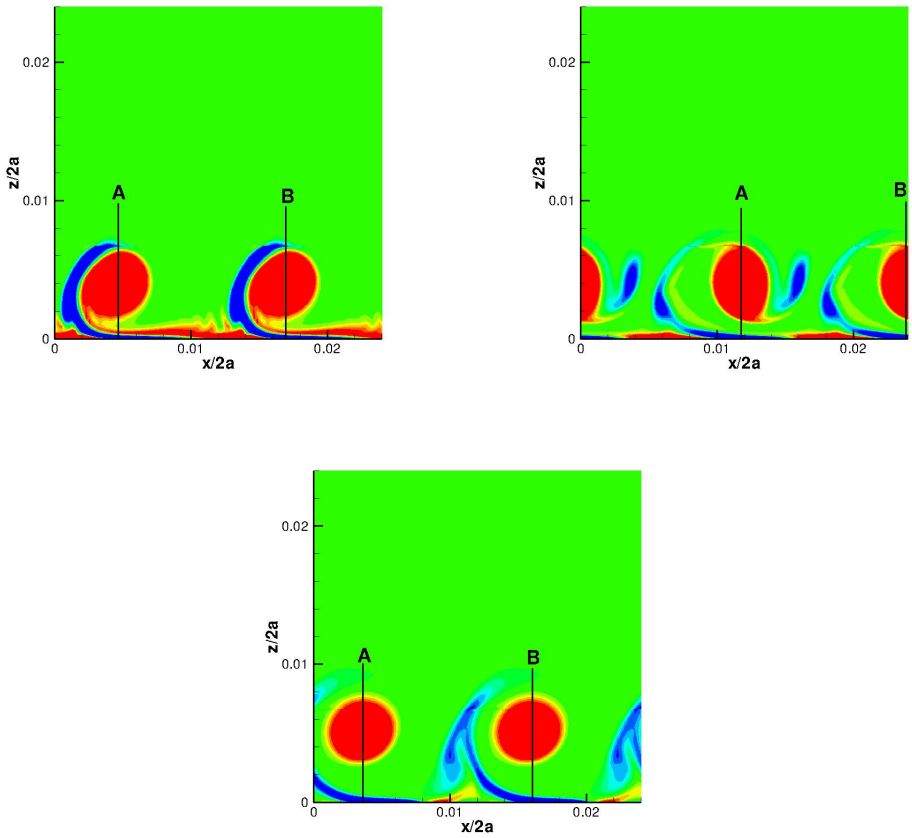

Figure 3.10: Visualization of the movement of two simulated vortex tubes, A and B, at Re = 6.5×10^5. The colored contours present the vorticity contour at different phases. The upper left panel is taken at $\omega\tau = 82°$; the upper right panel at $\omega\tau = 90°$; the lower panel at $\omega\tau = 110°$

tubes remains, the tubes also do not change the elevation too much, they more or less stay in a steady state, moving to the left. The diameter of the tubes is around 1 cm. The size and shape of the vortex tubes are very close to what is reported from Sumer *et al*. (2010)[21]. There is vorticity decaying occur once the vortex tubes are generated. Through figure 3.10 and figure 3.11, the vorticity magnitude of the vortex tubes are decreasing, as the upper limit of the vorticity magnitude for the vorticity contour is set to be 25 (1/s), there is no obvious

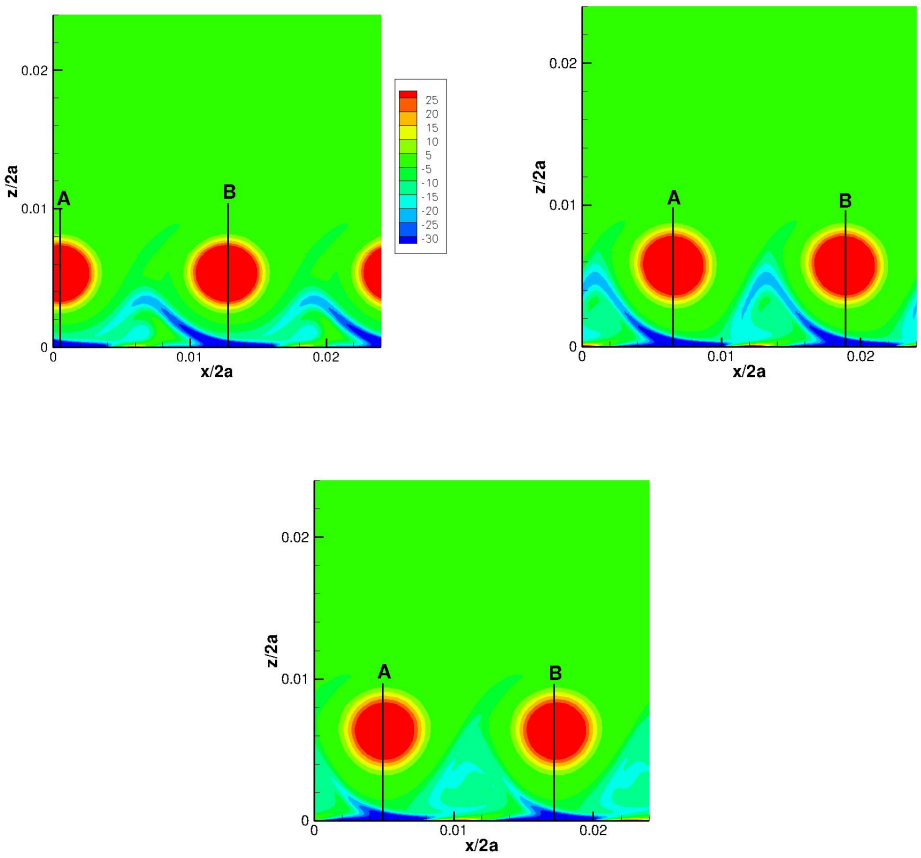

Figure 3.11: Visualization of the movement of two simulated vortex tubes, A and B, at Re = 6.5×10^5. The colored contours present the vorticity contour at different phases. The upper left panel at $\omega\tau$ = 134°; the upper right panel at $\omega\tau$ = 150° and the lower panel at $\omega\tau$ = 180°

change from the contour. Detailed evolution of the maximum vorticity will be discussed later.

The vortex tubes movement can be explained by looking at the phase speed of the shear instability, as discussed in Chapter 2. The phase speed of the shear instability can be approximately calculated by

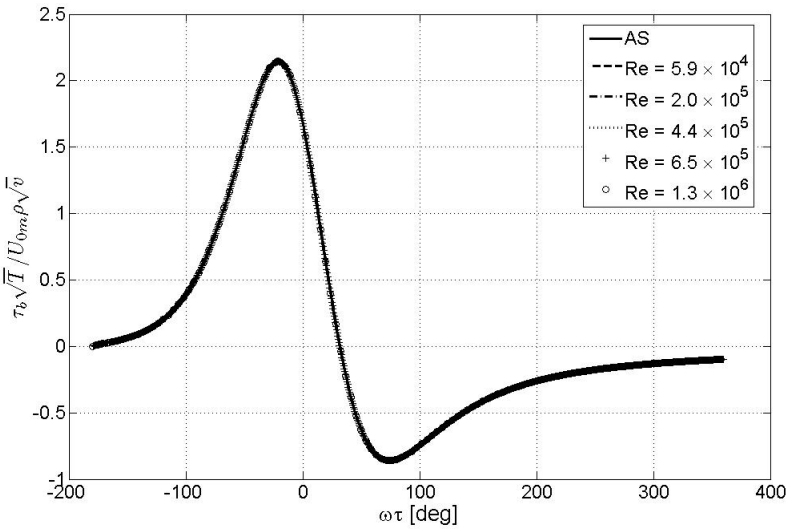

Figure 3.12: Phase variations of the normalized bed shear stress for different Reynolds numbers, and compared with the Analytical solution provided by Liu & Orfila (2004)[24].

$$\bar{u}_{vortex} = \frac{(u_{max} + u_{min})}{2} \tag{3.1}$$

As shown in figure 2.5, where the time history of the vortex tubes velocity is calculated and compared with the theoretical velocity of the shear instability at Re = 6.5×10^5.

3.3.3 An universal graph for the normalized bed shear stress

An universal graph for the normalized bed shear stress is produced after the bottom shear stress tests with different Reynolds number, while without introducing the perturbation velocity field. We find that if the bed shear stress is rescaled by $\rho\sqrt{\nu/T}/U_{0m}$, the time history of the normalized bottom shear stress for cases with different Reynolds numbers will lie on the same curve.

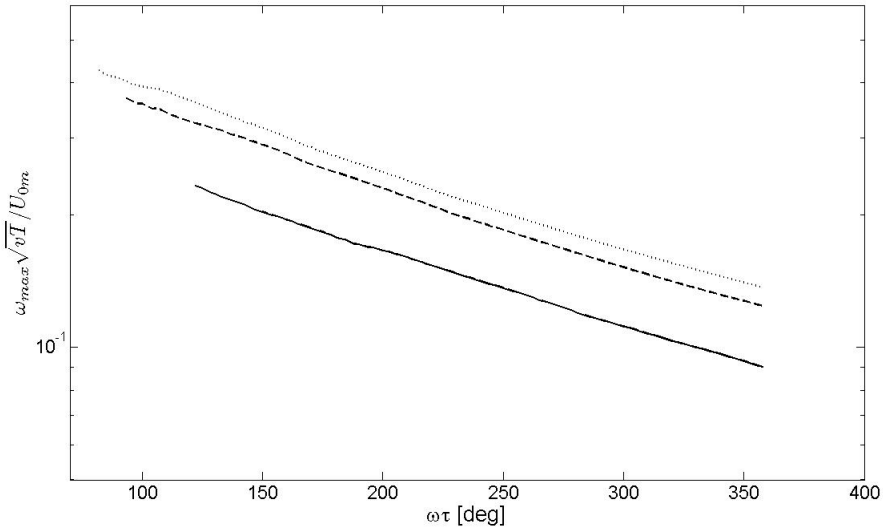

Figure 3.13: Phase variations of the normalized maximum vorticity for transitional flow cases. The solid line is at Re = 2.0×10^5, the dash line is at Re = 4.4×10^5, and the dot line is at Re = 6.5×10^5.

Figure 3.12 shows the phase variation of the normalized bed shear stress without perturbation velocity field for different Reynolds number. The range of the Reynolds number used here covers from laminar to transitional, and then to the turbulent flow region. Figure 3.12 shows that all curves match perfectly. This universal curve proves that the bed shear stress, and the boundary layer flow, is mainly effected by the difussion process. It will also be very useful to verify the set up of the cases used in this study by checking the bed shear stress without inserting perturbation velocity field.

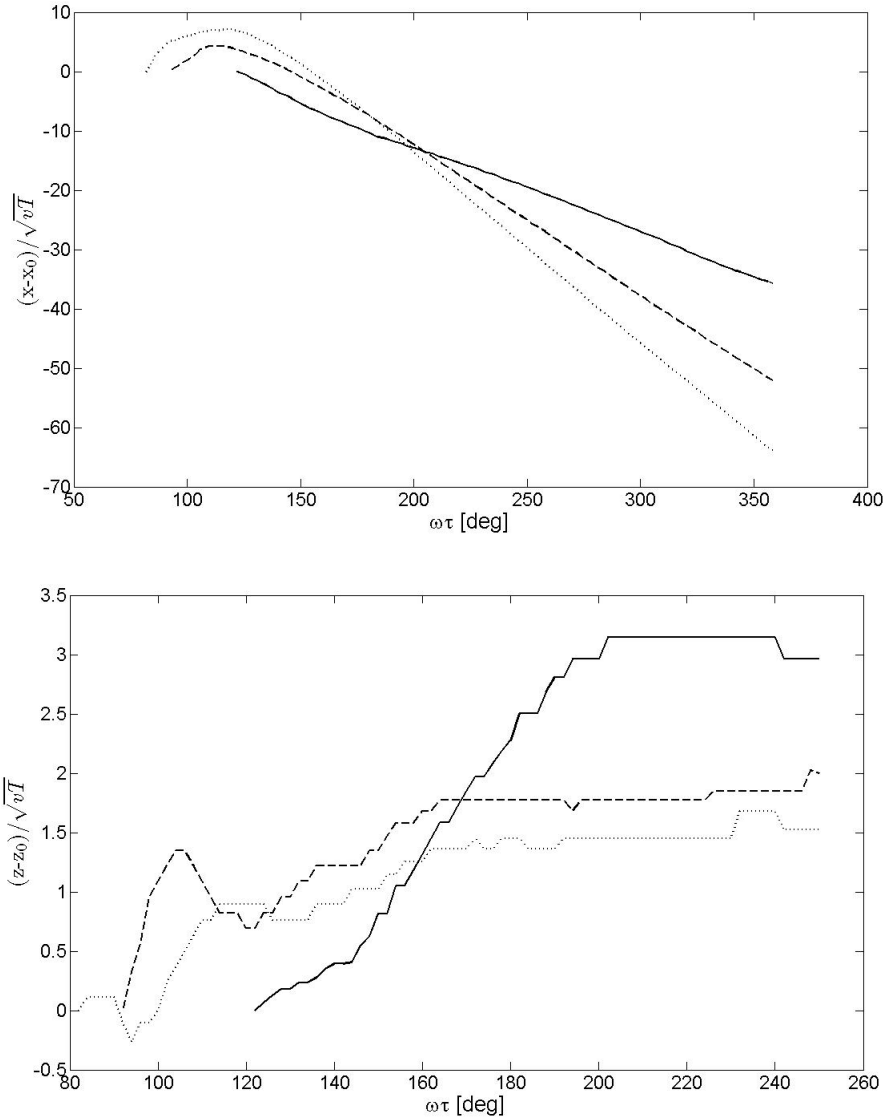

Figure 3.14: Phase variations of the normalized maximum vorticity for transitional flow cases. The solid line is at Re = 2.0×10^5, the dash line is at Re = 4.4×10^5, and the dot line is at Re = 6.5×10^5.

3.4 Discussion

3.4.1 Evolution of vortex tubes

The evolution of the vortex tubes generated by the K-H shear instability is discussed in this section. The maximum vorticity inside the vortex tubes is first

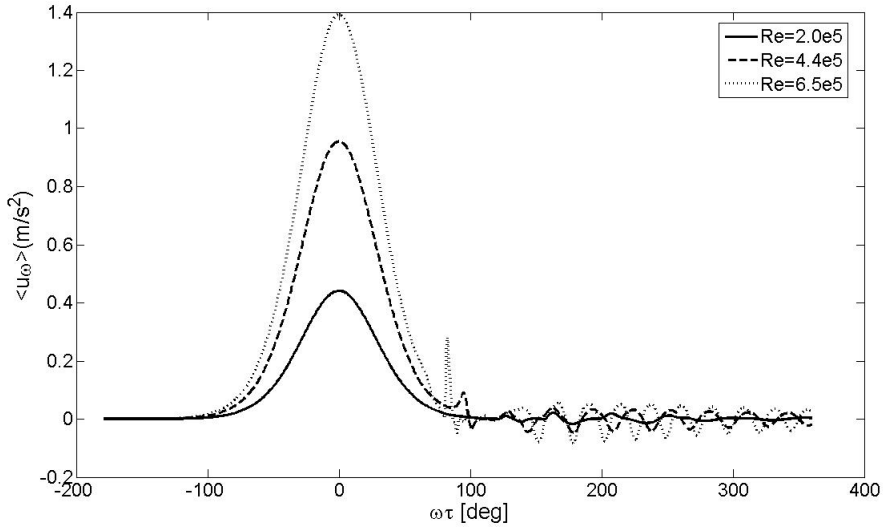

Figure 3.15: Time history of the horizontal vorticity flux

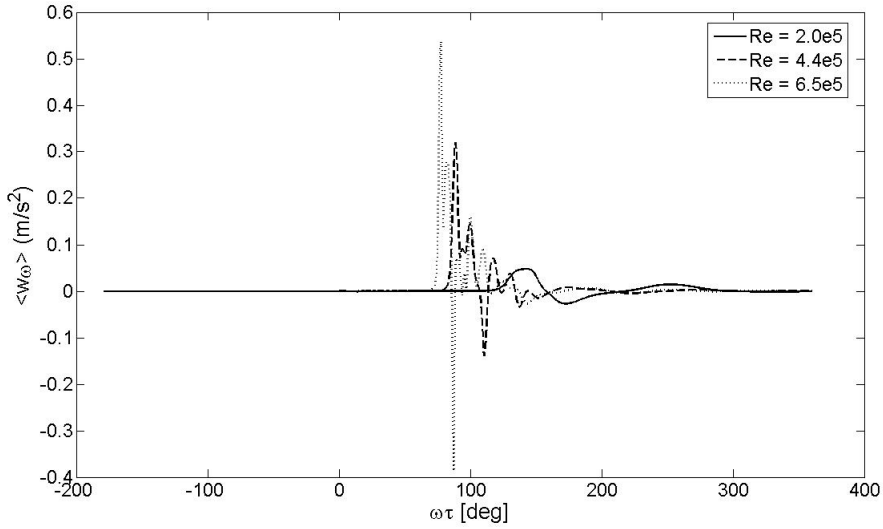

Figure 3.16: Time history of the vertical vorticity flux at z = 2.5 δ_m

calculated and taken as the center of the vortex tube. Noted that in this study two vortex tubes are simulated, two points with the same maximum vorticity value can be found. This study focuses on the left vortex tube, and the time history of the maximum vorticity is taken as the evolution of the vortex tubes

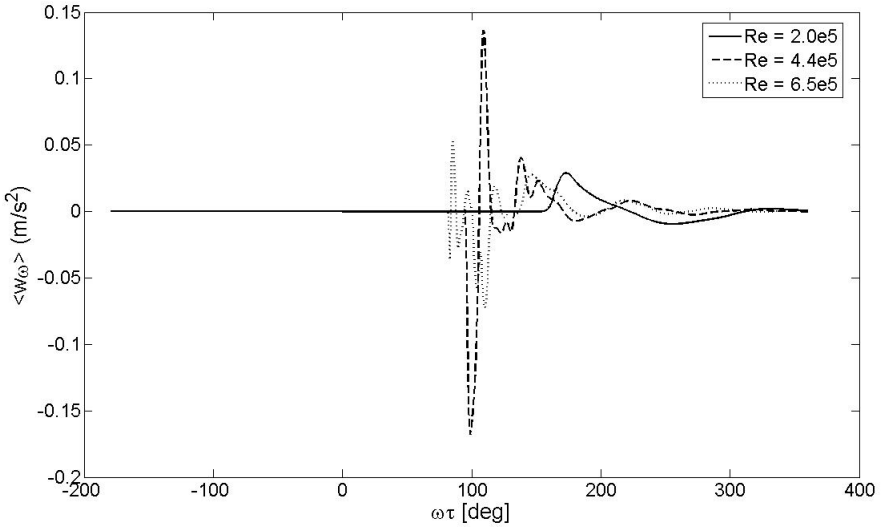

Figure 3.17: Time history of the vertical vorticity flux at z = 5 δ_m

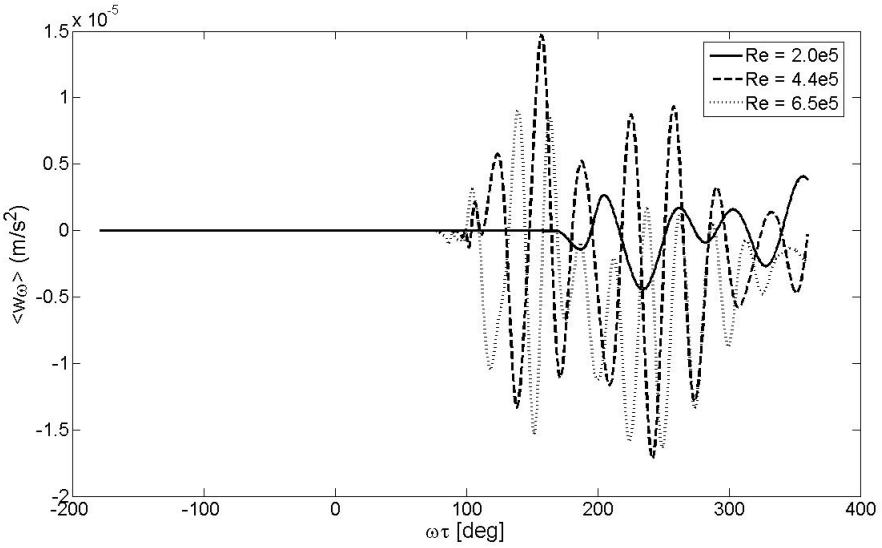

Figure 3.18: Time history of the vertical vorticity flux at z = 10 δ_m

and will be discussed in this section.

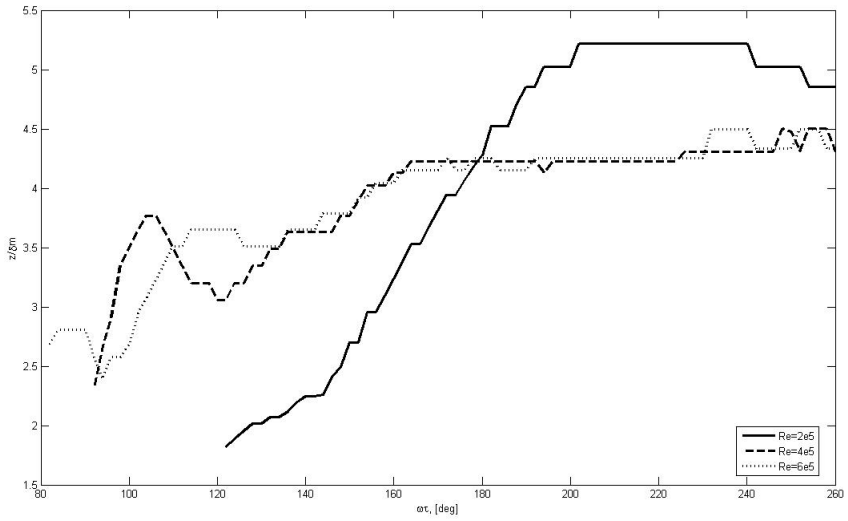

Figure 3.19: Phase variations of z-location of the maximum vorticity

The time history of the maximum vorticity

This section discusses the time history of the maximum vorticity for cases of Reynolds number 2.0×10^5, 4.4×10^5, and 6.5×10^5. Figure 3.13 shows the phase variation of the normalized maximum vorticity for these three cases. The maximum vorticity is rescaled by $\frac{\sqrt{\nu T}}{U_{0m}}$, and is shown in the log coordinate system. A general scratch of the time history of the maximum vorticity is that the maximum vorticity increases and reaches maximum at $\omega\tau$ = 0 °, and then starts to decay. As the flow is dominated by the diffusion effects, the rescaled plot will match perfectly on the growth stage. There will be difference for the maximum vorticity decay only when the vortex tubes are generated. As a results figure 3.13 only shows the time hisotry of the maximum vorticity after the vortex tubes are generated, that is, after $\omega\tau$ = 90 °. Figure 3.13 indicates that the decay of the maximum vorticity in the semi-log plot remain a straight line for all three cases. A lower Reynolds number case will has smaller quantities for the maximum

vorticity, as there is a slower flow in this case. However, the decay rate is found to be the same as exp(-0.004$\omega\tau$) for all the three cases. This indicates that the decay rate is a function of exponential ω, the frequency of the wave.

The trajectory of the maximum vorticity

In this section, the time history of the horizontal and vertical movement of the maximum vorticity is calculated and displayed in figure 3.14. The movement of the maximum vorticity is rescaled by $\sqrt{\nu T}$, which can be taken as the boundary layer thickness. Again by observation the time history begins to be recorded when the vortex tubes are detached from the bottom. The upper panel of figure 3.14 shows that for the later two cases, where Re = 4.4×10^5 and 6.5×10^5, the vortex tubes move to the right first before $\omega\tau$ = 130 °, then they move to the left of the simulation domain. This figure also indicates that for higher Reynolds number case, the slope of the horizontal movement, that is, the speed of the movement, is steeper, this means the speed is faster. The best fit for the horizontal speed of the maximum vorticity movement is shown in table 3.4. The lower panel of figure 3.14 shows the vertical movement of the maximum vorticity. This figure shows that the vortex tubes in these three cases raise more or less monotonically and then stay on an elevation, which is several times of the boundary layer thickness away from the bottom.

3.4.2 The Vorticity Flux discussion

This section discusses the time history of the horizontal and vertical vorticity flux for cases of Reynolds number 2.0×10^5, 4.4×10^5, and 6.5×10^5. To discuss the

Table 3.4: The horizontal speed of the maximum vorticity movement

Re	speed (m/s)
2.0×10^5	0.0174
4.4×10^5	0.0286
6.5×10^5	0.0367

Table 3.5: Horizontal and vertical location of the vorticity flux

Re	2×10^5	4×10^5	6×10^5
xlength	4.39	4.44	4.41
x (m)	0.0107	0.0128	0.0107
$2.5\delta_m$ (m)	0.007018	0.007098	0.00706
$5\delta_m$ (m)	0.014035	0.014195	0.01412
$105\delta_m$ (m)	0.02807	0.02839	0.02824

sediment transport affected by the vortex tubes generated by the shear instability in the bottom boundary layer caused by the surface solitary wave, the vorticity flux is considered. For the horizontal vorticity flux case, the equation can be written as:

$$HVF = \frac{\int_0^{zlength} u\omega \, dz}{zlength} \tag{3.2}$$

Where HVF is the horizontal vorticity flux, u is the horizontal velocity, ω is the vorticity, *zlength* is the vertical domain length, which is 0.145m for all cases. The horizontal location has to be determined in order to integrate along the vertical profile. In this study, the average of the horizontal movement of the vortex tube for each case is calculated and is taken as the horizontal location of

the vorticity flux. For the vertical vorticity flux, as the flux is moving away from the bottom, it is interesting for us to calculate the flux based on the distance of the vorticity thickness. 3 locations including 2.5 δ_m, 5 δ_m, and 10 δ_m away from the bottom are specified to calculate the flux. The vertical vorticity flux can be calculated as:

$$VVF = \frac{\int_0^{xlength} w\omega \, dx}{xlength} \tag{3.3}$$

Where VVF is the vertical vorticity flux, w is the vertical velocity, ω is the vorticity, *xlength* is the vertical domain length, which varies for all cases. Table 3.5 shows *xlength*, the calculated horizontal and vertical location for the 3 cases. Figure 3.15 shows the time history of the horizontal vorticity flux. The results indicate higher Reynolds number can create higher horizontal vorticity flux. A higher Reynolds number case also creates a stronger oscillation of the horizontal vorticity flux after the generation of the vortex tubes. These can be explained from that the maximum free stream velocity increases with a higher Reynolds number flow. Also vorticity is stronger as Reynolds number is bigger.

Figure 3.16 to figure 3.18 show the vertical vorticity flux at z= 2.5 δ_m, 5 δ_m, and 10 δ_m away from the bottom. General information from these figures is that a higher Reynolds number flow provides larger magnitude of the vertical vorticitiy flux. Vorticity fluxes for the three cases have larger values at 2.5 δ_m , have smaller values at 5 δ_m , much smaller values at 10 δ_m. This indicates that the vortex tubes are moving mainly around 2.5 δ_m. From figure 3.16, the figures indicate that for a smaller Reynolds number case, the vorticity flux starts later. This is because for smaller Reynolds number case, the vortex tubes generate later.

To analyze the vertical vortex flux, it will be interesting to also look at the z-location of the maximum vorticity, which indicates the trajectory of the vortex tubes. Figure 3.19 shows the phase variations of the maximum vorticity where the original location of the vortex tubes are shown to start at the elevation around 2~ 2.5 δ_m, moving upward before $\omega\tau$=200°, they remain stable at the elevation around 4.5~ 5 δ_m. But the vorticity and the horizontal velocity are much weaker at this phase.This can explain that there is larger vorticity flux at 2.5δ_m and smaller at 5δ_m.

CHAPTER 4

COHERENT STRUCTURES IN NON-SYMMETRIC TYPE SURFACE SOLITARY WAVE BOUNDARY LAYER

4.1 Cases description

To further discuss the impact of Tsunami on the shear instability in the bottom boundary layer, 3 cases with the non-symmetric solitary-type surface wave are designed. Case 5 from Sumer *et al*. (2010)[21] were chosen as the basic case and 2 other cases were designed with a non-symmetric-typed solitary wave.The wave period for the acceleration phase T_A remains the same for these three cases as 9.2s. The wave period for the deceleration period T_D are increasing from 1to 3 times of T_A for these 3 cases. Some important parameters are shown in table 4.1. Again 1.5 of the wave period is computed for the total numerical simulation duration for each case, where the simulation runs for half of the acceleration period first during the accerlation stage and then the simulation lasts for one deceratlation period. As the flow information such as vorticity thickness, the wavelength of the vortices in a shear layer stills needs to be calculated to construct the perturbation velocity field, the simlation therefore again is divided into two parts for each case. First a default simulation is done to design the perturbation velocity field, and then the perturbation velocity field is inserted to trigger the flow instability.

Table 4.1: Important parameters of the non-symmetric solitary wave cases

	case1	case2	case3
	$T_D = T_A$	$T_D = 2*T_A$	$T_D = 3*T_A$
T_A(s)	9.2	9.2	9.2
T_D (s)	9.2	18.4	27.6
U_{0m} (m/s)	0.36	0.36	0.36
Averaged T (s)	9.2	13.8	18.4

4.2 Results and Discussion

4.2.1 preliminary test to desing perturbation velocity field

Figure 4.1 shows the time history of the normailzed bed shear stress without perturbation velocity input. The bed shear stress is normalized by $\sqrt{\nu/T}/\rho U_{0m}$, where T is set to be T_A for all three cases. This figure indicates that for larger T_D, a smaller bottom shear stress is obtained. The momentum equation close to the bottom can be written as:

$$\frac{\partial u}{\partial t} = \nu \frac{\partial^2 u}{\partial z^2} = \frac{\partial \tau_b}{\partial z} \tag{4.1}$$

$$\tau_b = \int \frac{\partial u}{\partial t} dz \tag{4.2}$$

More,

$$\frac{\partial u}{\partial t} = 2U_{0m}\omega \tanh(\omega\tau) \tag{4.3}$$

Therefore with large wave period, the frequency is smaller, and then a smaller bed shear stress can be obtained.

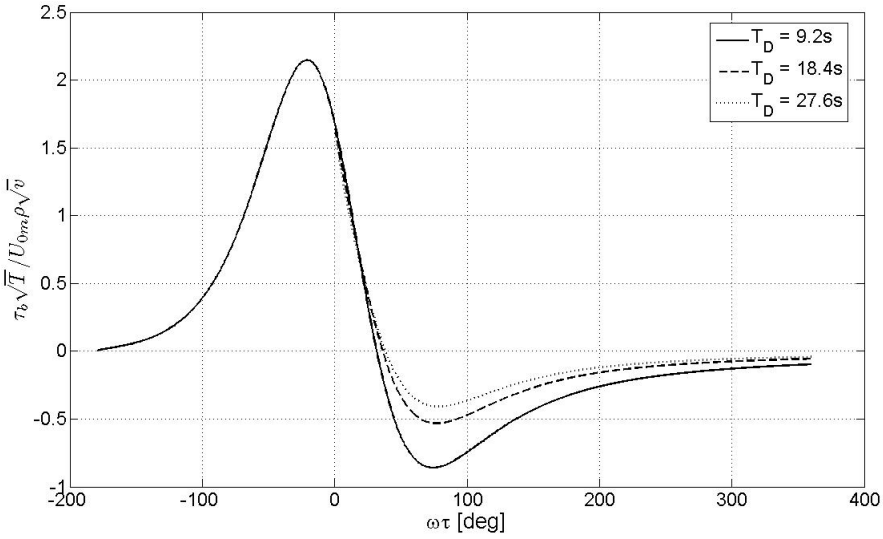

Figure 4.1: Time history of normalized bed shear stress without perturbation velocity input

4.2.2 Vortex tubes movement

With the information of flow properties, the perturbation velocity field can be designed for each case. Table 4.2 shows some fundamental properties for these cases. Figure 4.2 shows the time history of the normalized bed shear stress with perturbation velocity input, the bed shear stress is normalized by the same formula as in figure 4.1. This figure also shows that for higher wave period, there is smaller bottom shear stress. The oscillation of the bed shear stress after $\omega\tau$ = 40 ° is a clear evidence of the appearance of the vortex tubes.

Table 4.2: Summary of case information

case	T_D (s)	U_{0m} (m/s)	ν (m^2/s)	δ_ω (mm)	λ (cm)	$L_x(cm)$
1	9.2	0.36	1.E-06	2.81	2.19	4.38
2	18.4	0.36	1.E-06	3.56	2.78	5.56
3	27.6	0.36	1.E-06	4.18	3.27	6.54

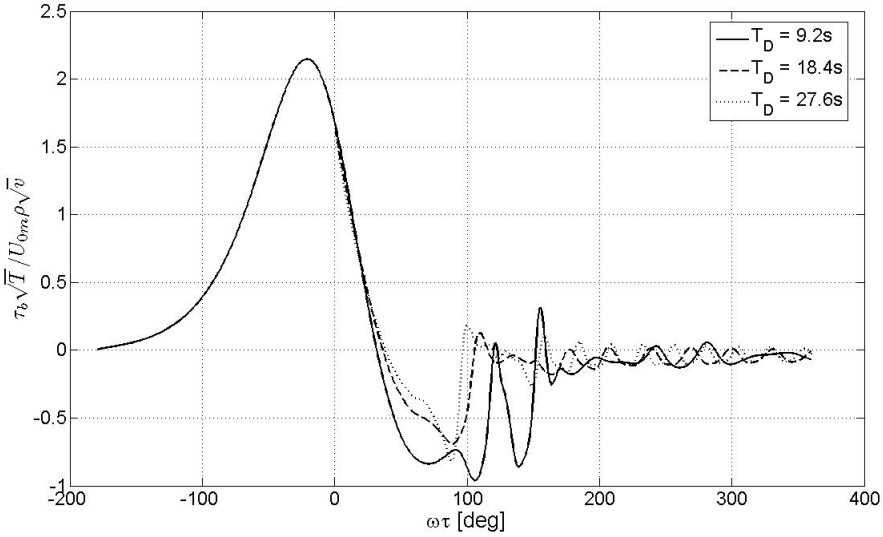

Figure 4.2: Time history of normailzed bed shear stress with perturbation velocity input

4.2.3 Evolution of vortex tubes

The evolution of the vortex tubes generated by the K-H shear instability for the non-symmetric surface solitary wave input cases is discussed in this section. The maximum vorticity inside the vortex tubes is first calculated and taken as the center of the vortex tube, and we describe the evolution and movement of the vortex tubes by looking at those properties of the maximum vorticity inside the vortex tubes. Noticed that again in this study the characteristics of the left vortex tube inside the simulation domain will be discussed.

Table 4.3: The decay rate of the three cases

case	T_A (s)	decay rate
1	9.2	$0.38exp(-0.0041\omega\tau)$
2	18.4	$0.47exp(-0.0048\omega\tau)$
3	27.6	$0.52exp(-0.0051\omega\tau)$

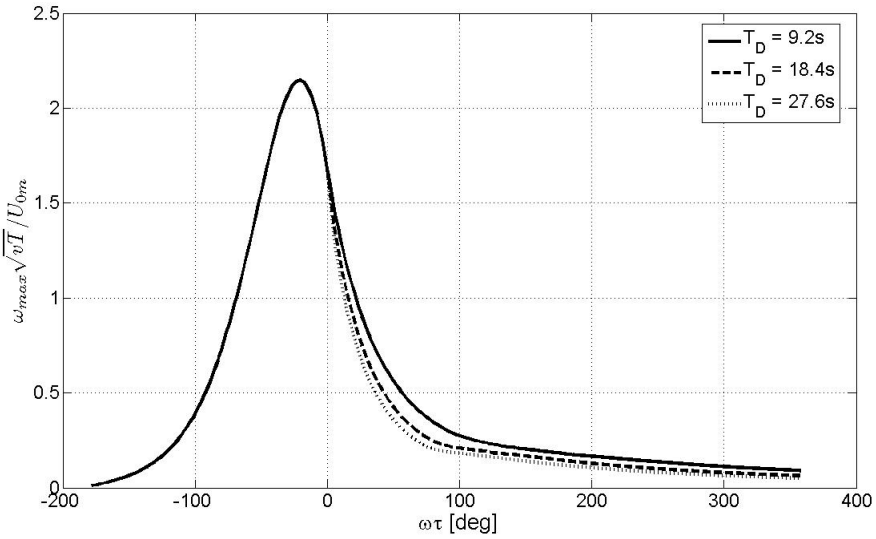

Figure 4.3: The phase variation of the maximum vorticity for the three cases

The time history of the maximum vorticity

By recording the phase variation of the maximum vorticity for each case, figure 4.3 shows that the normalzed maximum vorticity for these four cases remains the same before $\omega\tau$=0° , as we have the same T_A. The maximum vorticity drops in a different rate within different T_D during the deceleration stage. It is found that for larger T_D , the maximum vorticity decays faster. This indicates that for a larger wave period case, the reaction of the instability is stronger, therefore it decays faster.

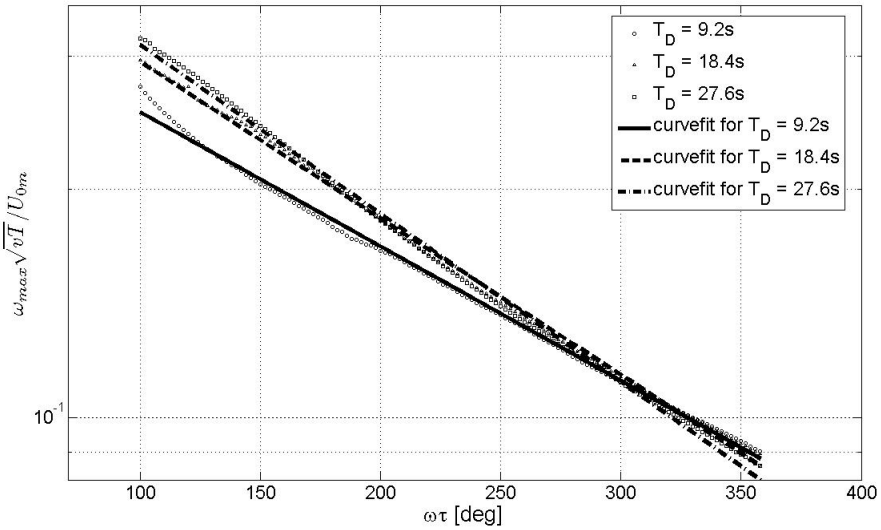

Figure 4.4: The decay rate of the maximum vorticity for the three cases

Table 4.4: Height of Descent(m)

	case2	case3	case4
Height of Descent (m)	0.0146	0.0152	0.0182

The maximum vorticity is normalized by $\sqrt{\nu T}/U_{0m}$, which indicates that the process is dominated by the viscous diffusion. Here T is set to be the acceleration wave period. Further observation was done to examine the decay rate of the maximum vorticity, as shown in figure 4.4. The normalized maximum vorticity is now rescaled by its own decerelation wave period as only the deceleration stage is discussed here, and is plotted in a log-normal coordinate system. A gaussian curvefitting is done for each case to find the decay rate for each case, which is shown in table 4.3. Table 4.3 indicates that for a larger acceleration wave period, there will be a larger decay rate, which is due to the more rapid flow condition. It will therefore take more energy while the vortex tubes are diminishing.

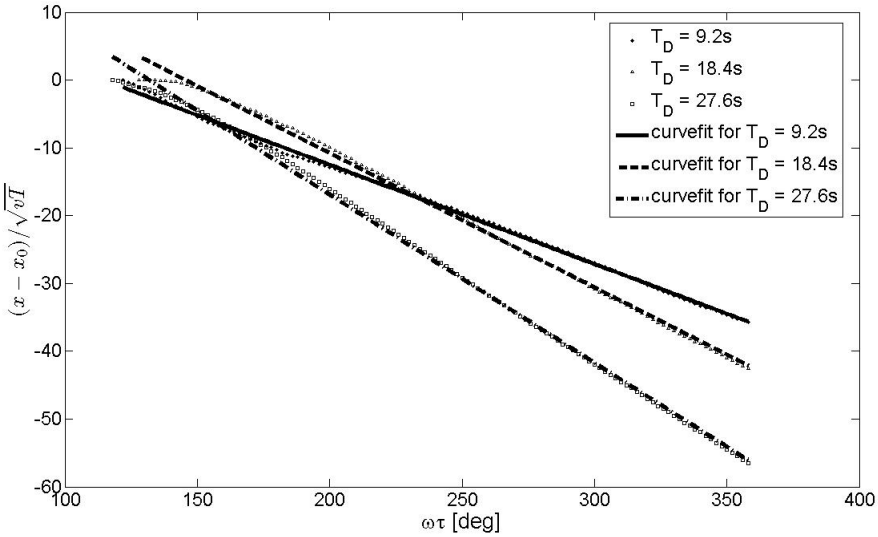

Figure 4.5: Horizontal trajectory of the maximum voritcity for these three cases

The trajectory of the maximum vorticity

In this section, the time history of the normalized horizontal movement of the maximum vorticity are calculated and displayed in figure 4.5. The movement of the maximum vorticity is rescaled by $\sqrt{\nu T}$, which can be taken as the boundary layer thickness. The deceleration wave period here again is used for normalization for each case as now we are focusing on the vortex tubes movement. By observation the time history begins to be recorded when the vortex tubes are detached from the bottom, which is around $\omega\tau$ = 120 °. Figure 4.5 shows that for a larger deceleration wave period, the slope of the horizontal movement becomes steeper, which means the vortex tubes move faster. The Gaussian curvefitting method is applied to find out the approximated horizontal velocity for each case. They are $\frac{x-x_0}{\sqrt{\nu t}}$ = -0.15 $\omega\tau$ + 16.76 for T_D = 9.2s, $\frac{x-x_0}{\sqrt{\nu t}}$ = -0.20 $\omega\tau$ + 28.80 for T_D = 18.4s, and $\frac{x-x_0}{\sqrt{\nu t}}$ = -0.25 $\omega\tau$ + 32.65 for T_D = 27.6s. By converting to the physical unit, the mean horizontal velocity for all three cases is around 0.017 m/s.

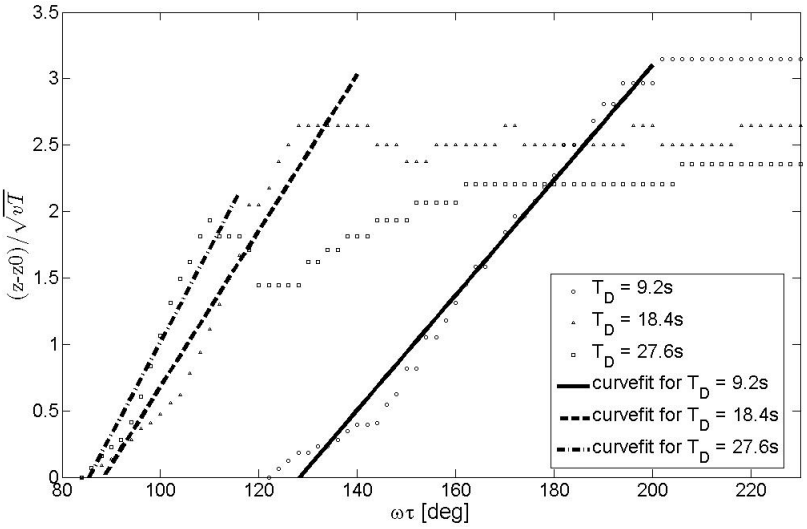

Figure 4.6: Vertical trajectory of the maximum voritcity for these three cases

Figure 4.6 shows the time history of the normalized vertical movement of the maximum vorticity. We use the same equation for the normalization. The gaussian curve fitting method is also applied for the vertical velocity calculation for each of the three cases. Marks in figure 4.6 are the numerical data grabbed from the model, lines are the curvefitting results. By looking at these dots for case T_D = 9.2s, the vertical trajectory of the maximum vorticity raised in constant speed from $\omega\tau$ = 120° to 200 °. For the other two cases as for larger deceleration wave period, the time for detachment is earlier, and the vortex tubes seem to stay at an elevation during for a while during the climbing period. For case T_D = 27.6s there is even for a period that the vortex tubes sink. To quantify the vertical movement, the Gaussian curve fitting method shows that for T_D = 9.2s, the approximation is $\frac{z-z_0}{\sqrt{vt}}$ = -0.43 $\omega\tau$ - 5.6, and $\frac{z-z_0}{\sqrt{vt}}$ = -0.06 $\omega\tau$ - 5.2 for T_D = 18.4s, $\frac{z-z_0}{\sqrt{vt}}$ = -0.07 $\omega\tau$ - 6.0 for T_D = 27.6s. The mean vertical velocity can be calculated by converting those formulas to physical unit, which is 0.005 m/s for all three cases. Table 4.3 shows the Height of Descent for each case. it indicates that for

larger wave period, the vortex tubes can reach higher elevation.

CHAPTER 5

CONCLUDING REMARKS

This study focuses on the fundemental issues of the boundary layer flow under a surface solitary wave. Previous study shows that as the Reynolds number increases, the boundary layer flow characteristics transform from being laminar to a transitional flow with the appearance of 2D laminar vortex tubes, and to the occurrence of turbulent spots. To exam the flow numerically in this study, a 2D pseudo-spectral multi-domain numerical model is applied, to study the coherent structures in wave boundary layer under the transitional flow regime. First the temporal behaviour of the bed shear stress is discussed. An universal curve is brought and proved to be fit for flow at different Reynolds numbers. This enhanced the recongnition of the flow behavior on the bottom boundary layer, which indicates that the diffusion process dominates the flow in the bottom boundary layer. The study also provides that as the idea environment is desinged in the numerical model, unlike in the laboratory where noises occur during experiment, a pertrubation velolcity field has to be design appropriately and inserted into the numerical cases to trigger the K-H instability for $2.0 \times 10^5 \leq \mathrm{Re} \leq 5\times 10^5$. The accurate 2-D numerical results provides analysis of the characteristics of the vortex tubes including the magitude, the evolution, the trajectory, the size and the shape of the coherent structure for different Reynolds numbers. Through the analysis of the vortex tubes evolution, we find that for different Reynolds number cases, the decay rate of the vortex tubes are a function of expemential of the wave frequency, $exp(\text{-}0.004\omega\tau)$ for all the three cases. The horizontal speed of the vortex tubes gets larger for the flow with a bigger Reynolds number.

Moreover, to refer the solitary wave to a more realistic tsunami-typed wave, the non-symmetric solitary waves with different length of the deceleration wave period (T_D) are designed and applied to test the wave boundary layer. The results show that within the same accelration wave period (T_A) but different T_D, the vortex tubes decay faster within a longer T_D. The horizontal speed of the vortex tubes are nearly the same, but a longer T_D has a longer transport period therefore the sediment has more potential tranported further with a larger T_D. For larger T_D the vortex tubes can reach a higher place, and again within the same T_A but different T_D the average vertical speeds for all cases do not have too much difference. This indicates that the movement of the vortex tubes are based on the energy accumulation from the acceleration stage, and a large T_D may provides a longer effecting period for the vortex tubes to the environment.

It is of interests to mention that there are differences between the U-tube setup and the wave boundary flows under a surface wave. In the U-tube experiment the horizontal velocity is uniform along the stream-wise direction, while in the wave boundary layer, the variation of the streamwise velocity does exist, which might effects the boundary layer flow study. It is also interesting to note that in real environment of the coastal ocean, the strong oncoming current plays an important role on the generation of the K-H shear instability in the bottom boundary layer. However, the oncoming current is not designed and included in this study. Therefore, it would be interesting to include the oncoming current to the future numerical analysis, to analyze the wave boundary layer behaviour in a more realistic situation.

BIBLIOGRAPHY

[1] G. K. Batchelor, H. K. Morffatt, and M. G. Worster. *Perspectives in Flluid Dynamics*. Cambridge University Press., 2000.

[2] J. P. Boyd. *Chebyshev and Fourier Spectral Methods.* Dover, 2001.

[3] C. Canuto, M. Y. Hussaini, A. Quarteroni, and T. A. Zang. *Spectral Methods in Fluid Dynamics*. Springer-Verlag Berline, 1998.

[4] S. Carstensen, B. M. Sumer, and J. Fredsoe. Coherent structures in wave boundary layers. part1. oscillation motion. *J. of Fluid Mech.*, 646:169–206, 2010.

[5] P. Costamagna, G. Vittori, and P. Blondeaux. Coherent structures in oscillatory boundary layers. *J. of Fluid Mech.*, 474:1–33, 2003.

[6] R. G. Dean and R. A. Dalrymple. *Water wave mechanics for engineers and scientists*. World Scientific, 1991.

[7] P. Diamessis and L. G. Redekopp. Numerical investigation of solitary internal wave-induced global instability in shallow water benthis boundary layers. *J. Phys. Oceanogr.*, 36(5):784–812, 2006.

[8] P. G. Drazin. *Introduction to hydrodynamic stability*. Cambridge texts in applied mathematics, 2002.

[9] J. Fredsoe and R. Deigaard. *Mechanics of Coastal Sediment Transport.* World Scientific, 1992.

[10] J. Fredsoe, B. M. Sumer, A. Kozakiewicz, L. H. C. Chua, and R. Deigaard. Effect of externally generated turbulence on wave boundary layer. *Coastal Engng.*, 49:155–183, 2003.

[11] D. Gottlieb and J. S. Hesthaven. Spectral methods for hyperbolic problems. *Journal of Computational and Applied Mathematics*, 128:83–131, 2001.

[12] J. L. Guermond and J. Shen. Velocity-correction projection methods for incompressible flows. *SIAM J. Numer. Anal*, 41:112–134, 2003.

[13] Yeh H., M. Francis, Peterson C., Katada T., Latha G., Ghadha R. K., Singh J. P., and Raghuraman G. Effects of the 2004 great sumatra tsunami: Southeast india coast. *J. Wtrwy, Port, Coastal, and Oc. Engng.*, 133:382–400, 2007.

[14] B. L. Jensen, B. M. Sumer, and J. Fredsoe. Turbulent oscillatory boundary layers at high reynolds numbers. *J. of Fluid Mech.*, 206:265–297, 1989.

[15] Huntington K., J. Bourgeois, Gelfenbaum G., Lynett P., Jaffe B., and and R. Weiss H., Yeh. Sandy signs of a tsunami's onshore depth and speed. eos. *Trans. Amer. Geophys. Union*, 88:577–578, 2007.

[16] Jankaew K., B. F. Atwater, Sawai Y., Choowong M., Charoentitirat T., Martin M., and A. Prebdergast. Medieval forewarning of the 2004 indian ocean tsunami in thailand. *Nature*, 455:07373, 2008.

[17] P. K. Kundu and I. M. Cohen. *Fluid Mechanics*. Elsevier Academic Press., 2004.

[18] J.-J. Lee, J. E. Skjelbreia, and F. Raichlen. measurement of velocities in solitary waves. *J. Wtrwy., Port, Coast., and Oc. Engrg*, 109:354–356, 1983.

[19] P. L.-F. Liu. Turbulent boundary-layer effects on transient long-wave propagation in shadow water. *Proc. Royal Soc. A*, 462:3431–34??, 2006.

[20] C. Lodahl, B. M. Sumer, and J. Fredsoe. Turbulent combined oscillatory flow and current in a pipe. *J. of Fluid Mech.*, 373:313–348, 1998.

[21] Sumer M., Jensen P., Sorensen L. B., Ferdsoe J., Liu P. L.-F., and S. Carstensen. Coherent structures in wave boundary layers. part 2. solitary motion. *J. Fluid Mech.*, 646:207–231, 2010.

[22] C. C. Mei. *The Applied Dynamics of Ocean Surface Waves.* John Wiley and Sons, 1983.

[23] Diamessis P. J., Domaradzki J.A., and Hesthaven J. S. A spectral multidomain penalty method model for the simulation of high reynolds number localized incompressible stratified turbulence. *J. Comp. Phys.*, 202:298–322, 2005.

[24] Liu P. L.-F. and Orfila A. Viscous effects on transient long wave propagation. *J. Fluid Mech.*, 602:83–92, 2004.

[25] Liu P. L.-F., P. Lynett, Fernando H., Jaffe B. E., Fritz H., Higman B., Morton R., Goff J., and Synolakis C. Observations by the international tsunami survey team in sri lanka. *Science*, 308:1595, 2005.

[26] Liu P. L.-F., Y.-S. Park, and Cowen E. A. Boundary layer flow and bed shear stress under a solitary wave. *J. Fluid Mech.*, 574:449–463, 2007.

[27] Tomoya Shibayama. *Coastal processes: Concepts in coastal engineering and their applications to multifarious environment*. World Scientific, 2009.

[28] W. D. Smyth and J. N. Moun. Length scales of turbulence in stably stratified mixing layers. *Phys. Fluids*, 12:1327–1342, 2000.

[29] S. A. Thorpe. *The turbulent ocean*. Cambridge University Press., 2005.

[30] G. Vittori and P. Blondeaux. Turbulent boundary layer under a solitary wave. *J. of Fluid Mech.*, 615:433–443, 2008.

[31] C. Winant and F. B. Browand. Vortex pairing : the mechanism of turbulent mixing-layer growth at moderate reynolds number. *J. of Fluid Mech.*, 63(2):237–255, 1974.